NASA Technical Memorandum 88217

An Experimental Investigation of the Aerodynamics of a NACA 64A010 Airfoil-Flap Combination With and Without Flap Oscillations

Part I. — Steady-State Characteristics

Donald A. Buell and Gerald N. Malcolm

July 1986

National Aeronautics and
Space Administration

NASA Technical Memorandum 88217

An Experimental Investigation of the Aerodynamics of a NACA 64A010 Airfoil-Flap Combination With and Without Flap Oscillations
Part I. — Steady-State Characteristics

Donald A. Buell,
Gerald N. Malcolm, Ames Research Center, Moffett Field, California

July 1986

National Aeronautics and
Space Administration

Ames Research Center
Moffett Field, California 94035

SUMMARY

A NACA 64A010 airfoil with a sealed-gap 1/4-chord flap was tested between splitter plates in the NASA Ames 11- by 11-Foot Transonic Wind Tunnel at Mach numbers from 0.50 to 0.85, and Reynolds numbers based on chord from 3 to 13 million. Although the main purpose of the test was to obtain unsteady pressure data with the flap oscillating, no unsteady data are presented in this paper. The steady-state data are presented and compared with other test data to provide a basis for evaluating the results.

Pressure data at two span stations are used to deduce early boundary-layer transition at the midspan at higher Mach numbers, angles of attack, and flap angles. The effects of flap angle on pressures, normal force, pitching moment, and hinge moment are also presented in this report. Mach number errors caused by the splitter-plate configuration and the angle of attack are evaluated using pressure measurements near the floor and ceiling of the wind tunnel.

INTRODUCTION

The desirability of being able to compute the compressible flow fields around aerodynamic bodies has led to an increasing number of experiments designed primarily to validate the computer codes. Applications to accelerating bodies (e.g., an oscillating wing) are particularly challenging, and are certainly essential for a comprehensive computational ability. Two-dimensional tests somewhat simplify the experiment-theory comparison by reducing the number of independent variables. An example of a two-dimensional test is reported in reference 1 by Davis and Malcolm, where a NACA 64A010 airfoil model was tested in a large wind tunnel at high Reynolds numbers to measure unsteady pressures caused by model oscillation. A sophisticated, hydraulically controlled, forced-oscillation apparatus was developed to produce a high-fidelity sinusoidal motion in pitch or heave.

Current interest in active controls makes the computation and validation of flows around an airfoil with a control surface particularly useful. Therefore, an experiment was devised to acquire data for an airfoil with a trailing-edge flap. This type of experiment has been performed very effectively by Tijdeman (ref. 2) for a NACA 64A006 airfoil at small surface incidences. It was decided to conduct a similar type of experiment but in a larger facility with an increased range of surface incidences, and with the thicker 64A010 profile that Davis and Malcolm had tested. A comparison with computed estimates was the primary goal, so, in addition

to measuring surface pressures, the experiment included a number of independent flow-field measurements by other contributing researchers that could also be used for code validation. These complementary measurements will be published separately.

This report provides a complete description of the model and the instrumentation, but the results are limited to the steady-state pressure data taken with the flap at fixed deflection angles. The effects of splitter-plate configuration, surface roughness of the model, Mach number, Reynolds number, angle of attack, and flap angle on the surface pressure distributions are the primary focus of the report. The report provides an evaluation of the data and serves as a basis for selecting and reporting the unsteady data in the future. Some of the unsteady data have already been published by the contributing researchers. Initial comparisons of the unsteady aerodynamic results with computed estimates are presented in reference 3 by Horiuti, Chyu, and Buell. Holographic interferograms of the flow over the airfoil can be found in reference 4 by Bachalo, and wake measurements are presented in reference 5 by Bodapati and Lee and in reference 6 by Owen.

NOMENCLATURE

c airfoil chord, 0.50 m (19.685 in)

c_f flap chord, 0.25 c

c plate splitter-plate chord, 2.84 m (112 in.)

Ch hinge-moment coefficient,

$$\int_{0.75}^{1} C_{p_l} (C/C_f)^2 (0.75 - x/c) d(x/c)$$

$$- \int_{0.75}^{1} C_{p_u} (C/C_f)^2 (0.75 - x/c) d(x/c)$$

Cm pitching-moment coefficient,

$$\int_0^1 C_{p_l} (0.25 - x/c) d(x/c) - \int_0^1 C_{p_u} (0.25 - x/c) d(x/c)$$

CN normal-force coefficient, $\int_0^1 C_{p_l} d(x/c) - \int_0^1 C_{p_u} d(x/c)$

C_p pressure coefficient, (p local - p)/q

C_{p_l} C_p on lower surface of wing

C_{p_u} C_p on upper surface of wing

f frequency of flap oscillation, Hz

k reduced frequency, $(\omega c)/(2V)$

M free-stream Mach number

M local local Mach number, $\sqrt{5\left[\frac{(1 + 0.2M^2)}{(1 + 0.7\ C_pM^2)^{2/7}} - 1\right]}$

p free-stream static pressure, N/m^2

q free-stream dynamic pressure, $1/2\rho V^2$, N/m^2

RN free-stream Reynolds number, $\rho Vc/\mu$

V free-stream velocity, m/sec

x streamwise coordinate, m, measured from leading edge

y airfoil-thickness coordinate, m, measured from chord line

z coordinate perpendicular to stream and span directions, m, measured from wing chord plane

α angle of attack, deg

δ flap angle, deg, measured from wing chord plane

$\bar{\delta}$ mean value of δ

ΔM effective increase in Mach number caused by wall interference

μ free-stream coefficient of viscosity, $N\text{-}sec/m^2$

ρ free-stream density, kg/m^3

ω circular frequency, $2\pi f$

FACILITY AND MODEL

The 11- by 11-Foot Transonic Wind Tunnel is a closed-return, variable-density facility with a 3.35 × 3.35 × 6.7 m (11 × 11 × 22 ft) test section enclosed in a 6-m-diam (20-ft) cylindrical pressure cell. The wall of the test section is ventilated with a baffled slot arrangement. The air is driven by a three-stage, axial-flow compressor powered by four induction motors with a maximum continuous combined output of 135 MW (180,000 hp). The Mach number can be varied continuously from 0.4 to 1.4, with the stagnation pressure variable from 50 kN/m to 225 kN/m (0.5 to 2.25 atm), resulting in Reynolds numbers from 6×10^6/m to 31×10^6/m.

The model was a NACA 64A010 airfoil with the coordinates as given in table 1. The first 70% of the wing was a steel shell with the upper surface unbroken from the leading edge to the 65% station. The trailing-edge flap was made of a graphite-epoxy composite with a cylindrical leading edge centered on the hinge line at the airfoil's 75% chord station. To seal the gap between the main airfoil section and the flap, metal strips 0.8 mm (0.032 in.) in thickness were embedded in the main airfoil section and rubbed on the flap as shown in figure 1. Pressure differences across the flap forced one of the strips more tightly against the flap to assist in the sealing. Unfortunately, the felt on the upper surface raised the metal strip slightly and caused a small discontinuity at the 75% chord station.

The support system for the airfoil was a pair of splitter plates which spanned the wind tunnel from floor to ceiling. The installation is shown in figures 2 and 3, and figures 4 through 7 show the pertinent dimensions. Each splitter plate contained a framed section which was thicker than the rest of the plate. This framed section housed a turntable to which the wing was rigidly attached. The wing angle of attack was varied by rotating the turntables with remotely controlled hydraulic cylinders. Each splitter plate also had a 21% chord trailing-edge flap that was manually adjustable. In addition, each turntable section had an inner and outer window that permitted optical transmissions through the plates. Pressure rails containing steady-state pressure orifices and high-response transducers were attached to the floor and ceiling to determine pressures outside the wind tunnel boundary layers. The normal 5% porosity of the test-section walls was not significantly altered by the pressure rails, but, as is shown in figure 2, some porosity was lost by a partial covering of the slots next to the splitter plates.

Figure 8 shows the lower front view of wing mounting. Access to the inside of the wing was by means of a removable panel on the lower surface. Figures 9 and 10 show the model in various states of disassembly. The pushrods which connected the wing flap to hydraulic actuators under the tunnel floor can be seen through the window in figure 11. These rods were constructed primarily from a graphite-epoxy material to provide high strength and stiffness with minimum weight. The servo-controlled hydraulic actuators were the same units used to oscillate the wing of reference 1. However, only two actuators were required for the present test, and the static-load biasing system was disconnected to give more precise control with the smaller flap loads.

INSTRUMENTATION

Both unsteady and "steady-state" (mean value) pressures were measured at the midspan of the wing and on the pressure rails attached to the ceiling and floor. In figure 6, the mid-span steady-state pressure orifices (pressure taps) actually consisted of 2 rows, 1.3 cm (0.5 in.) apart, with the orifices staggered. The same was true of the unsteady-pressure orifices. In addition, steady-state pressures were measured at the wing quarter-span station and on each side of both splitter plates. The locations are given in table 2.

The steady-state pressure orifices in the wing and pressure rails were 0.76 mm (0.030 in.) in diameter, while the unsteady pressure orifices were 1.27 mm (0.05 in.) in diameter. The large diameter of the latter orifices was selected for good frequency response but, as will be discussed later, was excessive for maintaining laminar flow. Differential transducers 2.4 mm (0.093 in.) in diameter were mounted on the axes of the orifices in the forward steel part of the wing, with each transducer diaphragm less than 2 mm from the surface. In the flap and pressure rails, the transducers were mounted at 90° to the orifice axis, 2 to 3 mm from the surface. Each transducer was located at the same chordwise station as a steady-state pressure orifice, and the reference side of the transducer was connected to the orifice through 9 m (30 ft) of tubing with an inside diameter of 0.71 mm (0.028 in.). This arrangement effectively damped out reference pressure fluctuations above 5 Hz, keeping the transducer in the calibrated pressure range around zero. It also permitted large amplifications of the dynamic signals because of the absence of large static offsets. The steady-state pressures (or mean of the unsteady pressures during flap oscillation) were routed to 24-port scanning valves for readout.

Flap position was determined by a linear variable differential transformer (LVDT) connected to the flap near the outer edge of the flap leading-edge radius at the 35% span station. The connector, a spring-loaded, plastic-toothed chain, was displaced fore and aft as the flap rotated. An independent check of flap position was computed using LVDTs on the flap actuators. LVDTs on the turntable actuators provided the angle-of-attack measurement. Loads and deflections were monitored by four strain gages and six accelerometers mounted at various locations on the flap, wing, splitter plates, and probe-support strut.

Most of the above signals, together with the temperature and pressures from the wind-tunnel operating instrumentation, were fed into a minicomputer through analog-to-digital converters for reduction, recording, and on-line plotting as shown in figure 12. The dynamic signals passed through a gate which was triggered to begin sampling the signals every 0.025 cycle of flap movement. The signals from the various sources were sampled in sequence at the rate of 200,000 samples/sec. The process was repeated 40 times for each cycle, and the voltages from each portion of the cycle were averaged over 100 cycles. The mean values from the scanning valves were determined from averages of 420 or more samples taken consecutively for each channel at the rate of 1115 samples/sec (over a whole number of cycles--at least

six--when the flap was oscillating). The computer also recorded the amplifier gains, which were automatically adjusted for optimum sensitivity at each new test condition. In addition, the computer initiated a timed cycle of dynamic-signal recording on three 32-channel FM analog recorders for later analysis of the high-frequency data.

The software for transducer calibration, data acquisition, storage, and plotting was developed over a period of 3 yr by Informatics General Corp. Parts of the code were utilized in two previous wind-tunnel tests during the development process. The organization of the code made possible its adaptation to widely varying unsteady-test requirements with a modest amount of reprogramming. Plots of either steady-state or unsteady data for a variety of parameters were available on demand immediately after a data-recording sequence.

The equipment required to make flow-field and wake measurements was supplied and operated by other researchers (ref. 4-6). These measurements included holographic interferometry of the flow field over and behind the wing (ref. 4), wake-probe measurements (ref. 5), and laser-doppler velocimeter measurements in the near wake (ref. 6). The wake-probe data included the mean and instantaneous values of the total and static pressures, and velocities derived from crossed hot film. The wake probe is shown in figure 13.

TESTS

After a few exploratory tests, the flaps on the splitter plates were each deflected outward 3.2° to relieve the tensile load on the wing. The load was caused by negative pressures on the outside of the turntable frames protruding from the splitter plates. After a few more runs, which revealed the effect of the splitter-plate flaps on the shock position, the splitter-plate flaps were moved back to a compromise position of 1.0° out, and were left in this position for the remainder of the test. The range of all the other variables is sumarized in table 3. The nominal Mach number was varied from 0.5 to 0.85. At the primary Mach number of 0.8, the Reynolds number based on chord length was varied from 3 to 12 million; the angle of attack, from 0 to 8; the flap angle, from -12° (up) to 8° (down); the amplitude of flap oscillation, from ±1° to ±6°; and the reduced frequency based on semi-chord, from 0 to 0.3. The table also notes those conditions for which holography, laser velocimetry, and wake-probe measurements were made.

REDUCTION OF DATA

Steady-state pressures, converted to standard pressure coefficients, comprise the basic data of this report. These pressures have also been integrated to approximate normal-force, pitching-moment, and hinge-moment coefficients. To obtain realistic flap loads, straight-line extrapolations were made from the two most-

forward-flap pressures forward to the hinge line on both the upper and lower surfaces. The trailing-edge pressure was taken as the average of straight-line extrapolations from the rearmost flap pressures on the upper and lower surfaces. The integration assumed straight lines between data points.

The free-stream static pressure was taken to be the average of the pressures on the inner surfaces of the splitter plates 0.1 chord above the wing (table 2). These orifices were about 1-1/2 chord lengths ahead of the wing leading edge. Mach number and dynamic pressure have been computed from this free-stream static pressure.

In general, no corrections have been made to the pressure coefficients for the known effects of the splitter-plate flaps, model lift, etc., because the primary use of the data--to check computational codes--is best satisfied by directly computing the airfoil characteristics in the wind tunnel environment using the measured pressure boundaries at the floor and ceiling (as in ref. 7 by King and Johnson). However, comparisons of the force and moment data with the data from other facilities are difficult without a consideration of the errors. To this end, Mach number corrections to the free-air condition have been approximated by the method of Mokry and Ohman (ref. 8), and are presented in figure 14. The effects of Reynolds number on the Mach number corrections were negligible. It should be noted that the method was slightly modified to bypass the fast Fourier transform procedures and substitute the original, somewhat simpler, formulation of the Dirichlet problem in reference 9. The corrections to dynamic pressure that are related to the Mach number corrections have also been applied to the integrated force and moment coefficients.

Similarly, corrections to the angle of attack caused by wind tunnel wall interference have been applied to the integrated force plots. These corrections were derived from reference 10, modified by the empiricisms of reference 11. The corrected angle of attack was taken as:

$$\alpha \text{ corr} = \alpha - 1.43 \text{ CN, deg}$$

RESULTS

The results are presented in figures 15 to 75 according to the index in Table 4.

Pressure and Mach Number Distributions

Mach number evaluation- The upper surface pressures are compared in figures 15 and 16 with data for the same airfoil with no flap (ref. 1), which was tested in the same facility. Differences between the two model installation involved model construction and splitter-plate configuration. The more aft position of the shock wave on the flap model is believed to be due to an effectively higher Mach number caused by the outward deflection of the splitter-plate flaps (undeflected in the original installation). This will be addressed more fully in the succeeding paragraphs. The negative forward pressures at zero angle of attack are related to the linearly

increasing error in thickness in the original wing model, as tabulated in reference 1. The pressure peak on the flap model near the hinge line (fig. 15) is due to a discontinuity in the gap covering as explained in the FACILITY AND MODEL section. The flow disturbance at the gap may possibly have caused some upstream movement of the shock wave, which would have reduced the discrepancy in shock position attributed to the splitter flaps. A comparison of upper and lower surface pressures is presented in a subsequent section, Effect of flap angle.

To illustrate the differences in Mach number gradient, pressures on the inner surface of the splitter plates in the two installations are compared in figures 17 and 18. Looking at the comparison from the 10% chord region to the 70% chord region, one can see a general overall divergence in the pressures, which indicates an acceleration in the present installation in comparison to the original. A somewhat more definitive comparison is made in figures 19 and 20, showing that a change in the splitter flap angle moves the shock location and changes the Mach number distribution on the ceiling. Even with the "normal" flap position, there is an increase in the Mach number from the free-stream measuring location, which is slightly upstream of the 0.2 (x/c) plate station, to the model. The method of reference 8 indicates that this is in excess of what might be expected from the model thickness effect and leads to the Mach number correction described in the REDUCTION OF DATA section.

With the proviso that the stated Mach numbers are less than the effective Mach numbers (by 0.015 at $M = 0.8$), the Mach-number effects at zero angle of attack are shown in figures 21 and 22. As Mach number increased, the usual aft movement of the shock wave occurred until a Mach number of 0.85 was reached. In this test condition, flap pressures decreased, indicating flow separation. In addition, the Mach number gradients on the floor and ceiling became quite large, as shown in figure 23. Because of the developing separation and the excessive Mach number gradients, the data for Mach numbers above 0.80 will not be considered in any detail.

Spanwise variations- A comparison between the midspan pressure measurements and the much more limited quarter-span measurements is shown in figures 24 through 26 for various test conditions. The comparison with biggest discrepancy (fig. 25), shows that the shock wave moved in opposite directions at the two span stations as the angle of attack was increased to 4°. The discrepancy is less at the higher Reynolds number (fig. 24), and is nonexistent at the lowest Reynolds number (fig. 26). This pattern is consistent with the presence of a transition trip at the midspan station, but not at the quarter-span station. It is conjectured that at the intermediate Reynolds numbers, something at the midspan caused a premature transition of the boundary layer from laminar to turbulent so that it grew more rapidly at the midspan, causing the shock to move forward. At the quarter-span station at these Reynolds numbers, the slightly favorable pressure gradient of the airfoil kept the boundary layer laminar up to or near the shock wave. At even higher Reynolds numbers, natural transition occurred earlier at the quarter-span station and moved the shock forward, while at low Reynolds numbers the midspan trip was insufficient to cause transition.

The mechanism necessary to trip the transition is believed to be the 1.27-mm (0.050-in.) orifices and/or cavity created by the recessed tranducers at the midspan. Somers et al. (ref. 12) show data that demonstrate how orifices can cause transition. The authors suggest "organ-piping" in the cavity as one possible cause of transition that is applicable in the present situation. This possibility could not be checked on the flap model because the instrumentation could not detect the high frequencies to be expected (70-kHz minimum according ref. 13).

It is reasonably certain that the spanwise pressure gradients aft of the shock led to three-dimensional flow, which, in turn, may have affected the aft pressures at the midspan. The three-dimensional nature of the flow may have been a contributing factor in the variance of the wake measurements noted in references 5 and 6. The localized nature of the transition trip makes it doubtful that the circulation around the airfoil was significantly affected. This conclusion is borne out by the lack of difference in the pressures forward of the shock. The available data (not shown) from the limited number of orifices on the lower surface show no differences between span stations.

A comparison of midspan and quarter-span pressures for other test conditions is given in figures 27 through 31. At a Mach number of 0.85 (fig. 27), pressure differences at the two span stations were not observed, possibly because the shock was aft of the quarter-span orifices. The differences were much smaller at a Mach number of 0.75 (fig. 28) and were nonexistent at a Mach number of 0.50 (fig. 29). Figure 30 shows that more positive flap angles greatly amplified the pressure differences between the two stations. The figure also illustrates the result (at $\delta = -4°$) that the quarter-span station sometimes had a better pressure recovery aft of the shock than the midspan station. Figure 31 shows the somewhat unexpected result that the large effects of Reynolds number persisted to an angle of attack of 8°.

Figures 32 through 34 and 35 through 37 present pressure distributions above the wing on the inside and outside, respectively, of one splitter plate. The effects of angle of attack are much the same at all Reynolds numbers, leading one to conclude that boundary layer transition and separation the plates were not greatly different at the various Reynolds numbers. Other data below the wing and on the opposite splitter plate showed similar effects.

Effects of Reynolds number- The apparent effect of Reynolds number at an angle of attack of 4° is shown in figures 38 through 40 for three Mach numbers. Recognizing that the midspan boundary-layer was probably tripped by the transducer orifices at the higher angles of attack, Reynolds numbers, and Mach numbers, one can conclude that the pressure distributions at those conditions tend to represent artificially high Reynolds numbers. Thus, in figure 38, the pressure distributions for Reynolds numbers of 6.5 and 12.5 million are very similar from the leading edge of the airfoil to the separated region near the 70% chord station. The effects of Reynolds number at smaller angles of attack (not shown) were negligible.

Effects of angle of attack- Figure 41 shows the effect of the angle of attack on the midspan pressures at a Mach number of 0.80. As explained above, the splitter

flaps created longitudinal gradients which made the effective Mach number at zero angle of attack greater than the nominal values, and moved the shock wave too far aft. In addition, figure 42 shows that there was an increasing Mach number gradient on both floor and ceiling as the angle of attack increased. The gradients are in excess of those expected from airfoil lift in free air and lead to the wall corrections presented in figure 14. Thus, the effective Mach number at an angle of attack of 8° was almost 0.85. The angle-of-attack effect is, incidentally, a situation which one expects with most wind tunnel models. Data for angles of attack of 4° and larger are also modified by the roughness effects of the transducer orifices.

Effect of flap angle- The effects of flap angle on the pressure distribution on both upper and lower surfaces are shown for Mach numbers of 0.80, 0.75, and 0.50 at the intermediate Reynolds number in figures 43 through 48 and 51 through 64. Flap effects at a Mach number of 0.80 and an angle of attack of 4° are also shown for the highest Reynolds number (fig. 49 and 50). One can see in figure 43 the steady progression of the shock wave to the rear as the flap angle increased, until separation developed (δ = +8°). (The critical pressure coefficient for this Mach number is -0.435.) Figure 44 shows a similar shock wave movement on the lower surface as flap angle was decreased to -4° (equivalent to +4° for the upper surface pressures). Definition of the more aft shock positions is hampered by a somewhat sparse distribution of pressure orifices. However, it appears that the more aft shock locations were farther forward on the lower surface than on the upper, for equivalent flap angles, probably because of a rougher lower surface.

In figure 43, the flow separation is indicated for flap angles as small as 4°. The pressures aft of the 80% chord station were very nearly the same on the upper (fig. 43) and lower (fig. 44) surfaces for equivalent flap angles, despite the upper surface discontinuity. Attached flow was obtained at both 0° and -4° flap angle when the angle of attack was 2° (figs. 45 and 46). Figures 47 and 48 indicate that an angle of attack of 4° was sufficient to separate the flow on one of the surfaces at all flap angles. The same was true at the higher Reynolds number (figs. 49 and 50), although the flap was slightly more effective aft of the shock in producing lift changes. Severe separation at the higher angles of attack greatly reduced the upper surface contribution to flap effectiveness.

At the lower Mach number of 0.75, separation was delayed to greater flap deflections. At an angle of attack of 4°, there were two flap settings, -4° and -8° (figs. 56 and 57) with no significant separation. At a Mach number of 0.50, there was only minor separation evident, even at the highest angle of attack of 8°.

Integrated Forces and Moments

To make comparisons with other investigators, it was necessary to apply the corrections outlined in the REDUCTION OF DATA section. These corrections partially compensate for wind tunnel and splitter-plate wall interference.

Comparisons with other tests- Figures 65 and 66 present comparisons of the integrated force and moment coefficients with the earlier splitter-plate test of

reference 1 (figs. 17 and 18), and with small-scale data obtained in the Ames 2- by 2-Foot Wind Tunnel (refs. 14 and 15). Corrections for the small-scale data are empirical, while the data from reference 1 have angle-of-attack corrections computed according to references 10 and 11. The most obvious difference between the flap model and the others is a large slope of the pitching-moment curve. The large slope can be traced primarily to the more rearward shock location caused by the splitter flaps. The magnitude of the effect makes clear the sensitivity of the results to wind tunnel environment and emphasizes the advisability of using measured pressure boundary conditions in a computation of the flow.

The presence of increased separation at the higher Reynolds numbers tended to balance the more aft shock position at low Reynolds numbers with the result that on the flap model the pitching characteristics were nearly the same for all Reynolds numbers.

Variation with flap angle- The pitching-moment and hinge-moment characteristics are shown in figures 67 through 75 with the flap angle as the primary variable. Despite the changes from subcritical to supercritical flow, and from unseparated to separated flow, the variation of pitching-moment coefficient with normal-force coefficient is nearly linear except at the Mach number of 0.75 (fig. 68). Here, there is a transition from the lower slopes of the high Mach number data (fig. 67) to the higher slopes of the low Mach number data (fig. 69). As noted previously, the Reynolds number effect is minimal.

The variation of hinge-moment with flap angle is much less regular (fig. 70, for example) except at the low Mach number (fig. 75). The Reynolds number effects are large at the higher angles of attack (figs. 72 and 73) where the hypothesized early transition occurred on the upper surface. The early transition hastened flow separation on the flap, which resulted in the negative increments of hinge moment. At these conditions the hinge-moment data would be a poor parameter for comparisons.

CONCLUSIONS

A NACA 64A-010 airfoil with a 1/4-chord trailing-edge flap has been tested, primarily to obtain data on the effects of flap oscillation. To provide a basis for evaluating the results, steady-state data taken with the flap at fixed deflection angles have been examined in detail and compared with data from other tests. The following conclusions are drawn from these steady-state data:

1. The splitter-plate configuration produced an acceleration which made the effective Mach number higher than the nominal. As a result, the shock wave was further aft and the slope of pitching moment versus lift was more negative than that found by other researchers. The measured pressures near the floor and ceiling provide a pressure-boundary condition which must be included in the flow computation if the Mach number is to be properly matched.

2. Increasing the angle of attack also caused an increase in the effective Mach number. This, too, can be accounted for by use of the measured pressure boundary conditions.

3. At Reynolds numbers of 6 million or above, at a Mach number of 0.80, and at the higher angles of attack and flap angles, it is deduced that the transducer orifices caused premature boundary-layer transition at the midspan station. The resulting pressure distributions from the leading edge of the airfoil to the shock-wave location are thought to be representative of artifically high Reynolds numbers. The effect of the three-dimensional flow aft of the shock wave is unknown. At a Mach number of 0.80, the apparent Reynolds number effects are minimal on normal force and pitching moment, but are anomalous in the hinge-moment data.

4. At a nominal Mach number of 0.80, attached flow was achieved only at angles of attack less than 4° and flap angles within the range from -4° to +2°. The range of angles for attached flow increased as Mach number decreased. At a Mach number of 0.50, only minor separation was detected at any of the angles tested.

REFERENCES

1. Davis, Sanford S.; and Malcolm, Gerald N.: Experimental Unsteady Aerodynamics of Conventional and Supercritical Airfoils. NASA TM 81221, 1980.

2. Tijdeman, H.: Investigations of the Transonic Flow around Oscillating Airfoils. NLF TR 77090U, 1977.

3. Horiuti, K.; Chyu, W. J.; and Buell, D. A.: Unsteady, Transonic Flow Computations for an Airfoil with an Oscillating Flap. AIAA Paper 84-1562, June 1984.

4. Bachalo, William: Flow-Field Measurements on an Airfoil with an Oscillating Trailing-Edge Flap Using Holographic Interferometry. NASA CR 166603, 1984.

5. Bodapati, S.; and Lee, C. S.: Unsteady Wake Measurements of an Oscillating Flap at Transonic Speeds. AIAA Paper 84-1563, June 1984.

6. Owen, Kevin: Wake Profile Measurements of Fixed and Oscillating Flaps. NASA CR 166602, 1984.

7. King, L. S.; and Johnson, D. A.: Calculations of Transonic Flow About an Airfoil in a Wind Tunnel. AIAA Paper 80-1366, July 1980.

8. Mokry, M.; and Ohman, L. H.: Application of the Fast Fourier Transform to Two-Dimensional Wind Tunnel Wall Interference. J. Aircraft, vol. 17, no. 6, 1980, pp. 402-408.

9. Powers, D. L.: Boundary Value Problems, Academic Press, New York, 1972, pp. 110-117.

10. Pindzola, M.; and Lo, C. F.: Boundary Interference at Subsonic Speeds in Wind Tunnels with Ventilated Walls. AEDC TR-69-47, May 1969.

11. Barnwell, Richard W.: Design and Performance Evaluation of Slotted Walls for Two-Dimensional Wind Tunnels. NASA TM 78648, 1978.

12. Somers, Dan M.; Stack, John P.; and Harvey, William D.: Influence of Surface Static-Pressure Orifices on Boundary-Layer Transition. NASA TM 84492, 1982.

13. Rossiter, J. E.: Wind-Tunnel Experiments on the Flow Over Rectangular Cavities at Subsonic and Transonic Speeds. R & M 3438, Aeronautical Research Council, 1966.

14. Johnson, D. A.; and Bachalo, W. D.: Transonic Flow About a Two-Dimensional Airfoil - Inviscid and Turbulent Flow Properties. AIAA Paper 78-1117, July 1978.

15. Gross, Anthony R.; and Steinle, Frank W., Jr.: Pressure Data from a 64A010 Airfoil at Transonic Speeds in Heavy Gas Media of Ratio of Specific Heats from 1.67 to 1.12. NASA TM X-62468, 1975.

TABLE 1.- 64A010 AIRFOIL COORDINATES

x/c	Design y/c	Measured y/c		x/c	Design y/c	Measured y/c	
		upper	lower			upper	lower
0.0	0.0			0.4	0.04995	0.0498	-0.0498
.005	.00804	0.0077	-0.0086	.45	.04894	.0487	-.0488
.0075	.00969	.0094	-.0101	.5	.04684	.0466	-.0465
.0125	.01225	.0119	-.0125	.55	.04388	.0437	-.0437
.025	.01688	.0165	-.0170	.6	.04021	.0400	-.0399
.05	.02327	.0229	-.0233	.65	.03597	.036	-.036
.075	.02807	.0277	-.0281	.7	.03127	.032	-.031
.1	.03199	.0317	-.0319	.75	.02623	.028/27	-.026
.15	.03813	.0379	-.0381	.8	.02103	.022	-.021
.2	.04272	.0425	-.0426	.85	.01582	.016	-.016
.25	.04602	.0459	-.0459	.9	.01062	.011	-.011
.3	.04837	.0482	-.0482	.95	.00541	.005	-.005
.35	.04968	.0495	-.0495	1.0	.00021	0.000	0.000

TABLE 2.- PRESSURE-MEASURED LOCATIONS

Wing, x/c				Pressure rails, (x/c) plate	
Midspan (transducers & s. s. orif.)		Quarter-span (s. s. orif. only)		(transducers & s. s. orif.)	
Upper	Lower	Upper	Lower	Ceiling	Floor
0.000				0.225	0.210
.025				.313	.298
.050	0.050	0.050		.401	.386
.075				.489	.474
.100	.100	.100		.577[a]	.562
.125				.664	.649
.150	.150			.752	.737
.175				plenum	plenum
.200		.200	.200		
.225				z/c=	
.250	.250			3.067	-2.977
.275					
.300	.300	.300			
.325					
.350	.350				
.375					
.400	.400	.400	.400		
.425					
.450	.450				
.475				Wake probe	
.500	.500	.500		(transducers only)	
.525				Total & Static	
.550	.550			x/c 1.05 to 2.00	
.575				z/c -0.4 to 1.0	
.600	.600	.600	.600		
.625					
.643	.643				
.674		.675			
.705					
.768	.762				
.797	.793				
.849	.849				
.896	.895				
.950	.946				

Pressure-measure locations for wing

[a]Inoperative transducer

TABLE 2. - Continued.

Section	Port splitter				Starboard splitter			
	Inside		Outside		Inside		Outside	
	(x/c) pl	z/c	(x/c) pl	(x/c) z/c	(x/c) pl	z/c	pl	z/c
Upper	0.032	1.22	0.032	1.22	0.032	1.22	0.032	1.22
	.053		.053		.053		.044	
					.072		.072	
	.111		.111		.111			
	.124		.124		.124		.124	
	.138		.138		.138		.138	
	.151		.151		.151		.151	
	.214	1.52			.214	1.52		
	.259				.259		.259	1.17
	.304				.304			
	.348				.348		.346	
	.393				.393		.391	
	.438						.436	
	.482				.482			
	.527				.527			
	.571				.571			
	.616				.616		.669	
	.661				.661		.687	
	.705				.705		.709	
	.750				.750			
					.880	1.22	.880	1.22
					.901			
					.920		.920	
					.941		.941	
					.961			
					.979			

TABLE 2. - Concluded.

Section	Port splitter				Starboard splitter			
	Inside		Outside		Inside		Outside	
	(x/c) pl	z/c	(x/c) pl	z/c	(x/c) pl	z/c	(x/c) pl	z/c
Center	0.112	0.10			0.112	0.10		
	.124				.124			
	.138				.138			
	.151				.151			
			.012	-1.02	0.012	-1.02		
	0.032	-1.02	.032		.032		0.32	-1.02
	.053		.053		.053		.052	
Lower	.111		.111		.111		.111	
	.124				.124		.124	
	.138		.138		.138		.138	
	.151		.151				.151	
					.214	-1.52		
					.259			
					.304			
					.344			
					.616			
					.661			
					.705			
					.750			
			.901	-1.02	0.901	-1.02		

TABLE 3.- TEST VARIABLES - NOMINAL VALUES

M	RN/10^6	α, deg	$\bar{\delta}$ and δ, k = 0	Amplitude, deg k = 0.05	k = 0.1	k = 0.175	k = 0.3
0.50	5	0, 4, 8	-4, 0	2	2	2	
		0, 4	-12, -8, 4, 8				
		8	-12, -8, 4				
	10	0, 4	-4, 0	2	2	2	
.75	6	0, 4, 8	-8, -4, 0	2	2	2	
		0, 4	-12, 4, 8				
		8	-12, 4				
	12	0	0	2	2	2	
		0	-4				
		4	-4, 0	2	2	2	
.77 - .79	6	0	0				
.80	3	0, 4, 8	-4, 0	2	2	2	
		0, 4, 8	-8				
	6	0	(-4), (0)	1, 2, 4, 6	1, 2, 4, 6	1, (2), 4	1, 2
		0	-8, -2, 2, 4	2	2	2	
		0	-12, 8				
		2	-4, 0	1, 2, 4	1, 2, 4	1, 2, 4	1, 2
		2	-8	2	2	2	
		4	(-4), (0)	1, 2, 4, 6	1, 2, 4, 6	1, (2), 4	1, 2
		4	-8, -2, 2, 4	2	2	2	
		4	-12, 8				
		6	-4, 0	2	2	2	
		6	-8				
		8	0	1, 2, 4, 6	1, 2, 4, 6	1, 2, 4	1, 2
		8	-8, -4	2	2	2	
		8	-12, 4				

TABLE 3.- Concluded.

M	$RN/10^6$	α, deg	$\bar{\delta}$ and δ, k = 0	Amplitude, deg k = 0.05	k = 0.1	k = 0.175	k = 0.3
	12	0	0	1, 2	1, 2	1, 2	1, 2
		0	-2, 2, 4				
		4	-4, 0	1, 2, 4	1, 2, 4	1, 2, 4	1, 2
		4	-2, 2, 4				
.81 - .84	6	0, 4	0				
.85	7	0	-4, 0	1, 2, 4	1, 2, 4	1, 2, 4	
		0	-8	2	2	2	
		0	-12, 4, 8				
		2	-8, -4, 0	2	2	2	
		2	-12, 4, 8				
		4	-4, 0	1, 2, 4	1, 2, 4	1, 2, 4	
		4	-8	2	2	2	
		4	-12, 4				
	13	0	0				

◯ Optical & wake measurements

TABLE 4.- INDEX TO DATA FIGURES

Fig. no.	Title	M	$RN/10^6$	α, deg	δ, deg
Pressure and Mach no. distributions					
15 - 18	Comparisons with other test	0.8	12 - 13	0, 4	0
19 - 20	Effect of splitter flaps	.8	7	0	0
21 - 23	Effect of M	.75 - .85	7	0	0
24 - 37	Effect of span position	.5 - .85	3 - 13	0 - 8	- 4 to 4
38 - 40	Effect of RN	.5 - .8	3 - 13	4	0
41 - 42	Effect of α	.8	7	0 - 8	0
43 - 64	Effect of δ	.5 - .8	5 - 13	0 - 8	-12 to 8
Integrated forces and moments					
65 - 66	Comparisons with other tests	.8	2 - 13	0 - 8	0
67 - 69	Pitching moment	.5 - .8	3 - 13	0 - 8	-12 to 8
70 - 75	Hinge moment	.5 - .8	3 - 13	0 - 8	-12 to 8

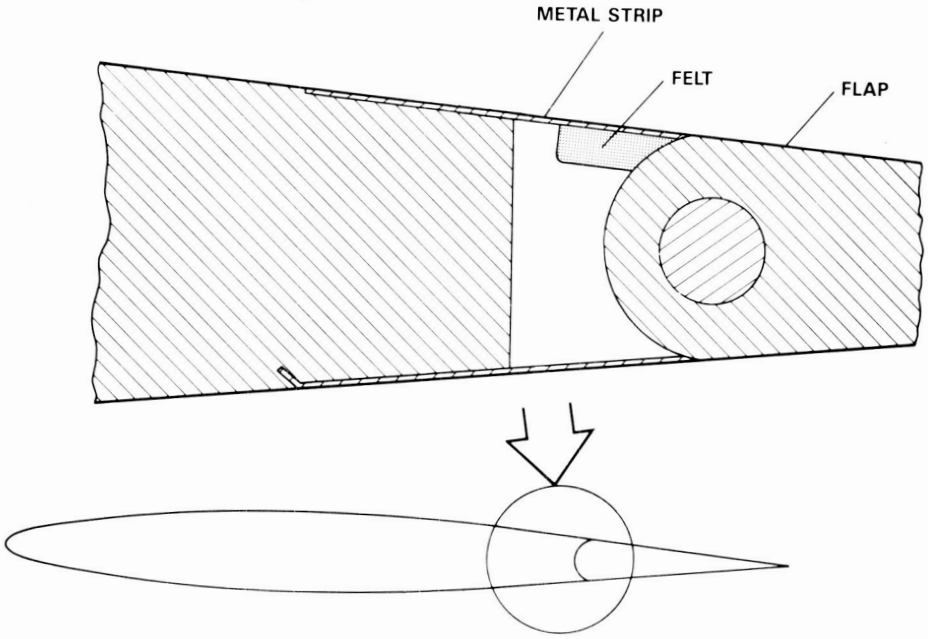

Figure 1.- Method of sealing the gap between the airfoil and flap.

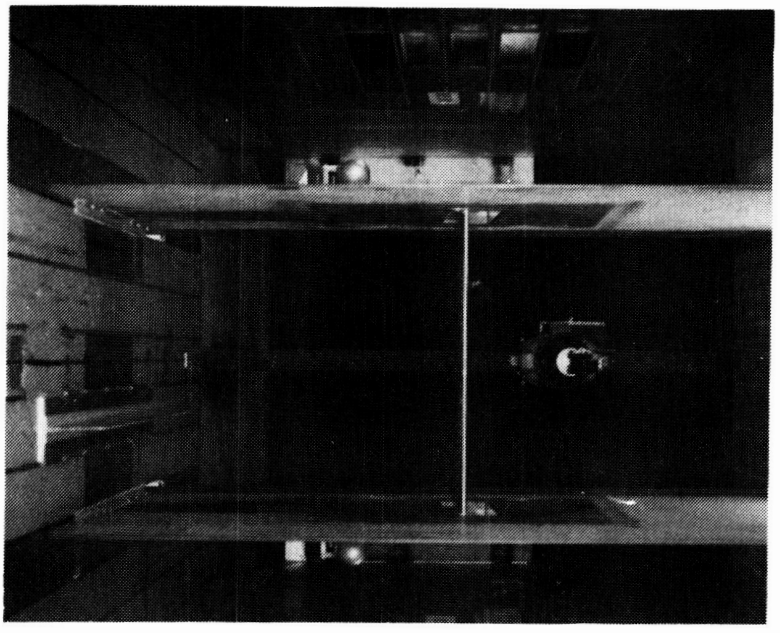

Figure 2.- Oscillating-flap model.

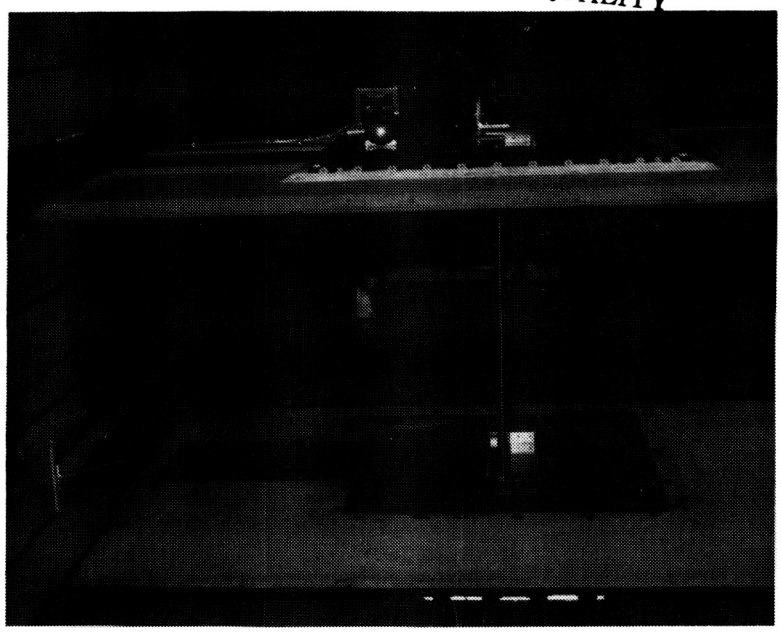

Figure 3.- Front side view of oscillating-flap model.

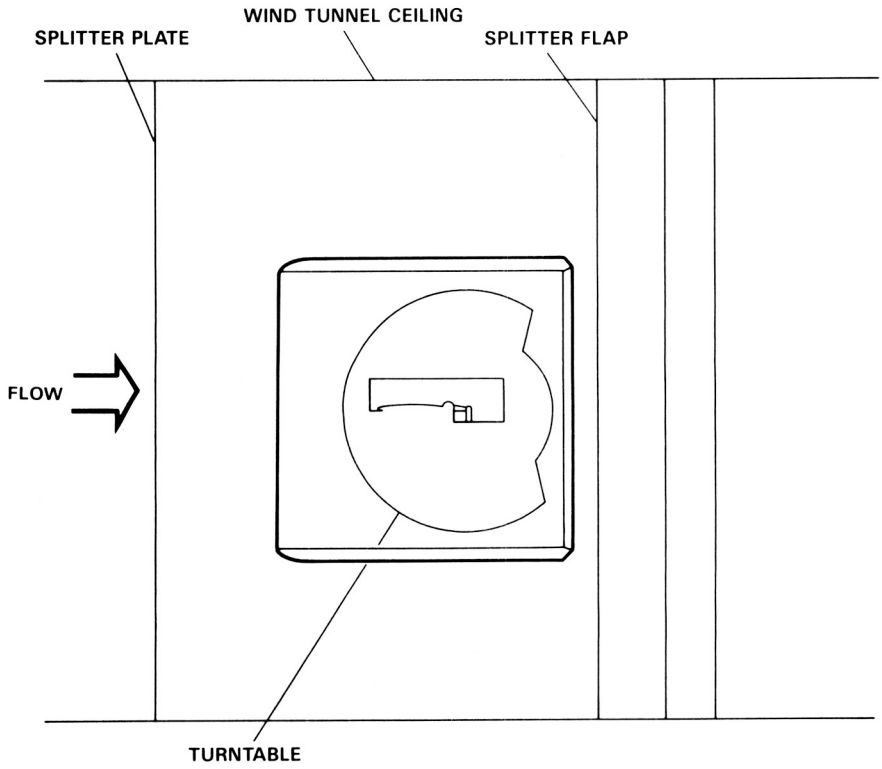

Figure 4.- Side view of the exterior surface of the splitter plates.

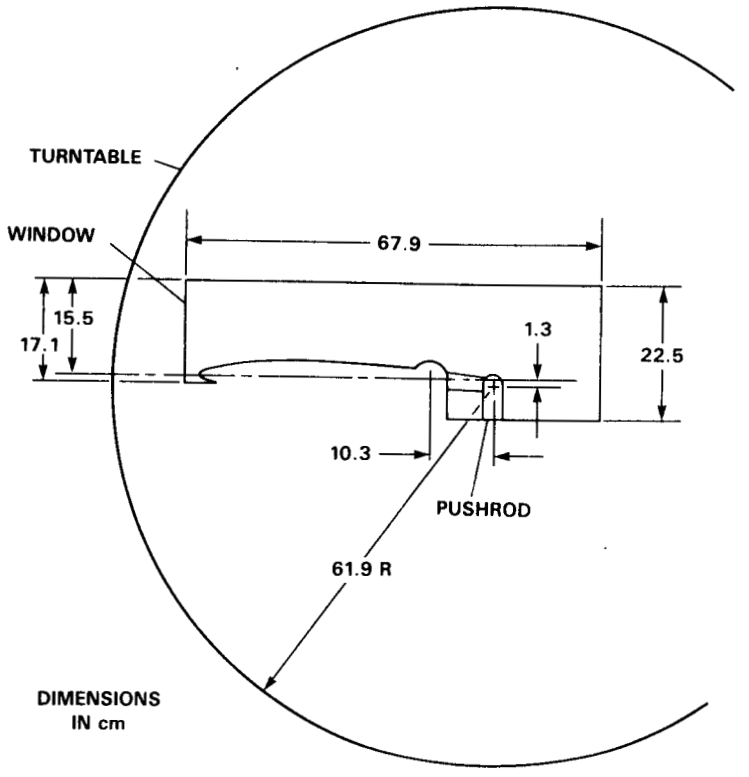

Figure 5.- Enlarged side view of one of the turntables, showing optical access to the flow over the airfoil.

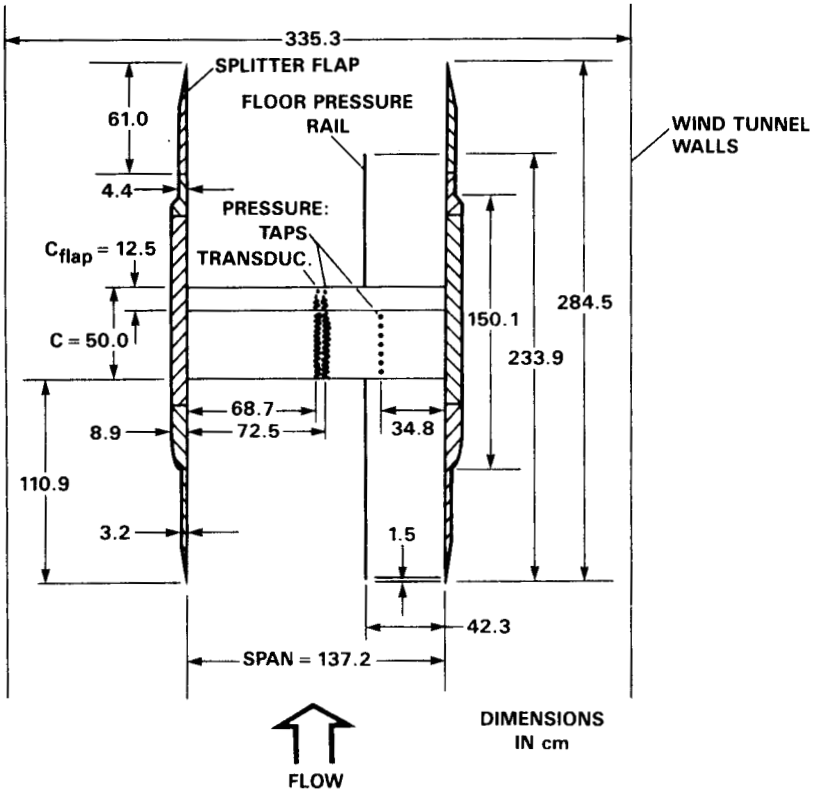

Figure 6.- Top sectional view of the model and splitter plates.

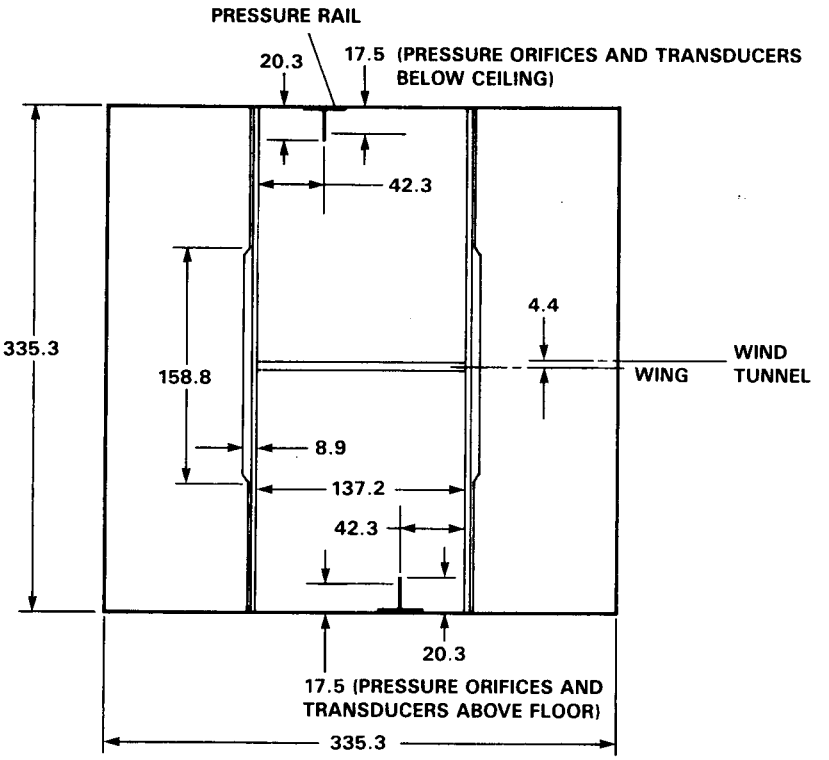

Figure 7.- Dimensions in the front view of the installation.

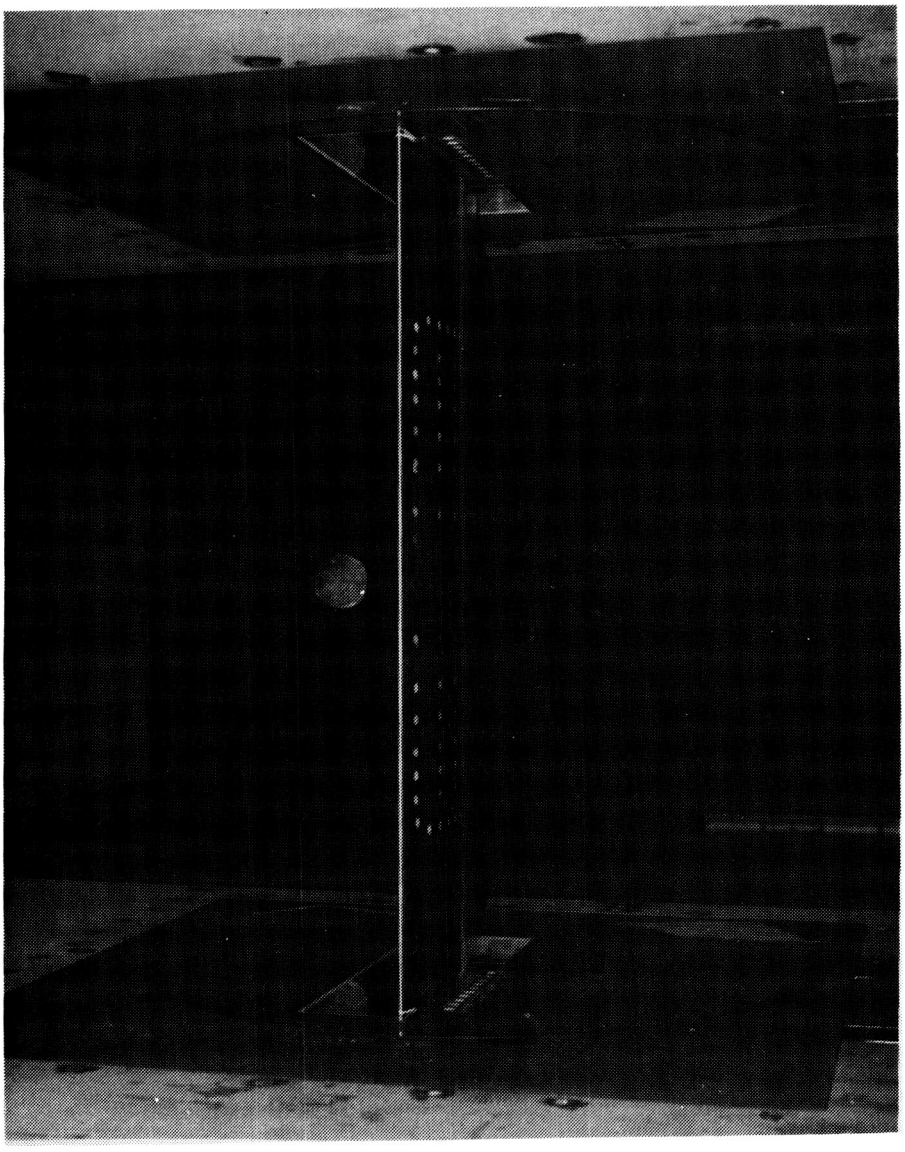

Figure 8.- Lower front view of oscillating-flap model.

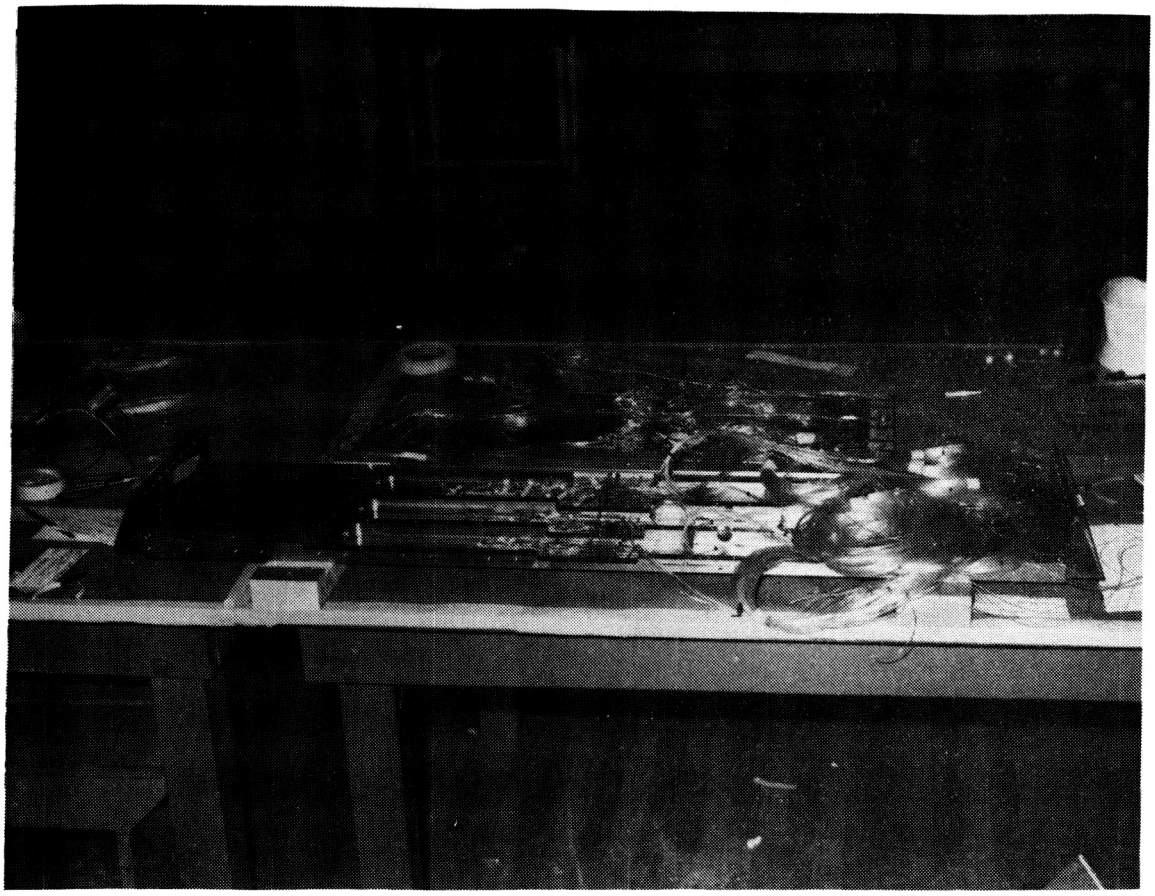

Figure 9.- View of disassembled wing from oscillating-flap model.

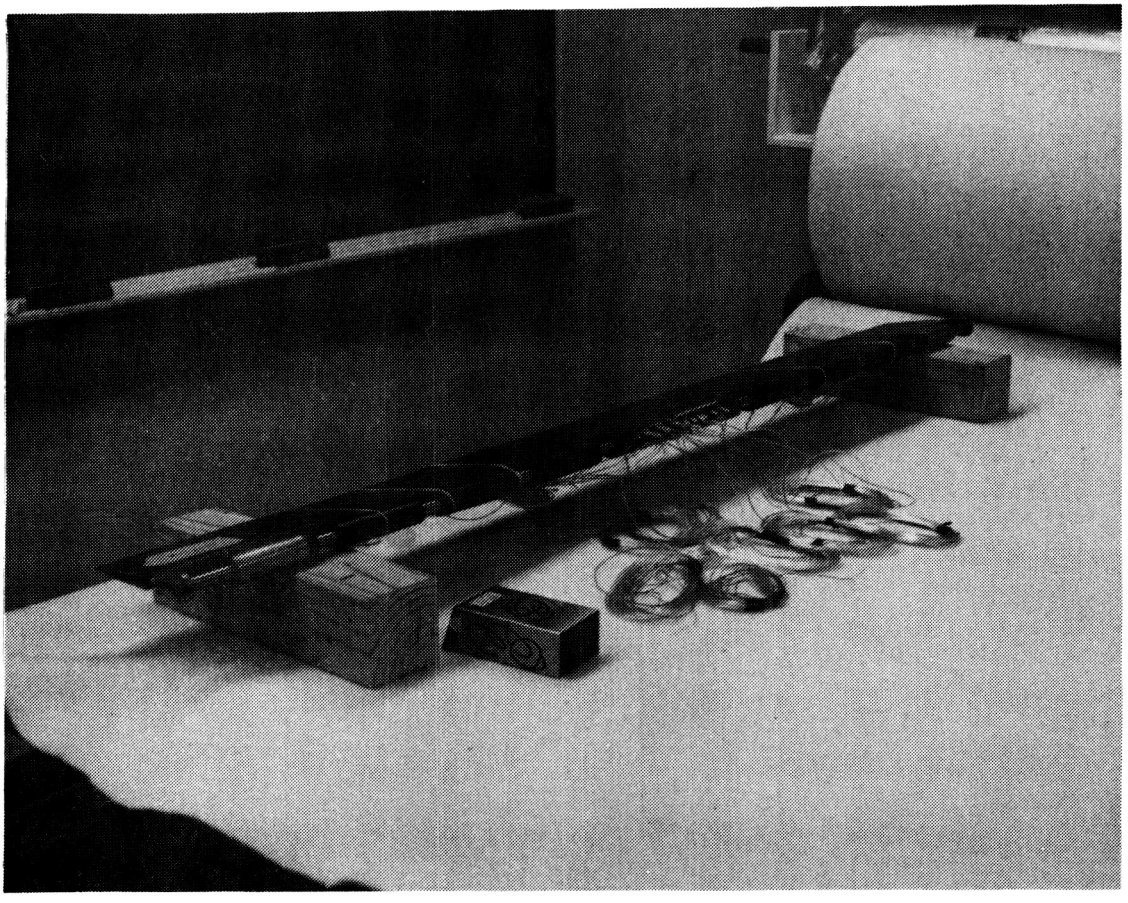

Figure 10.- View of flap before assembly.

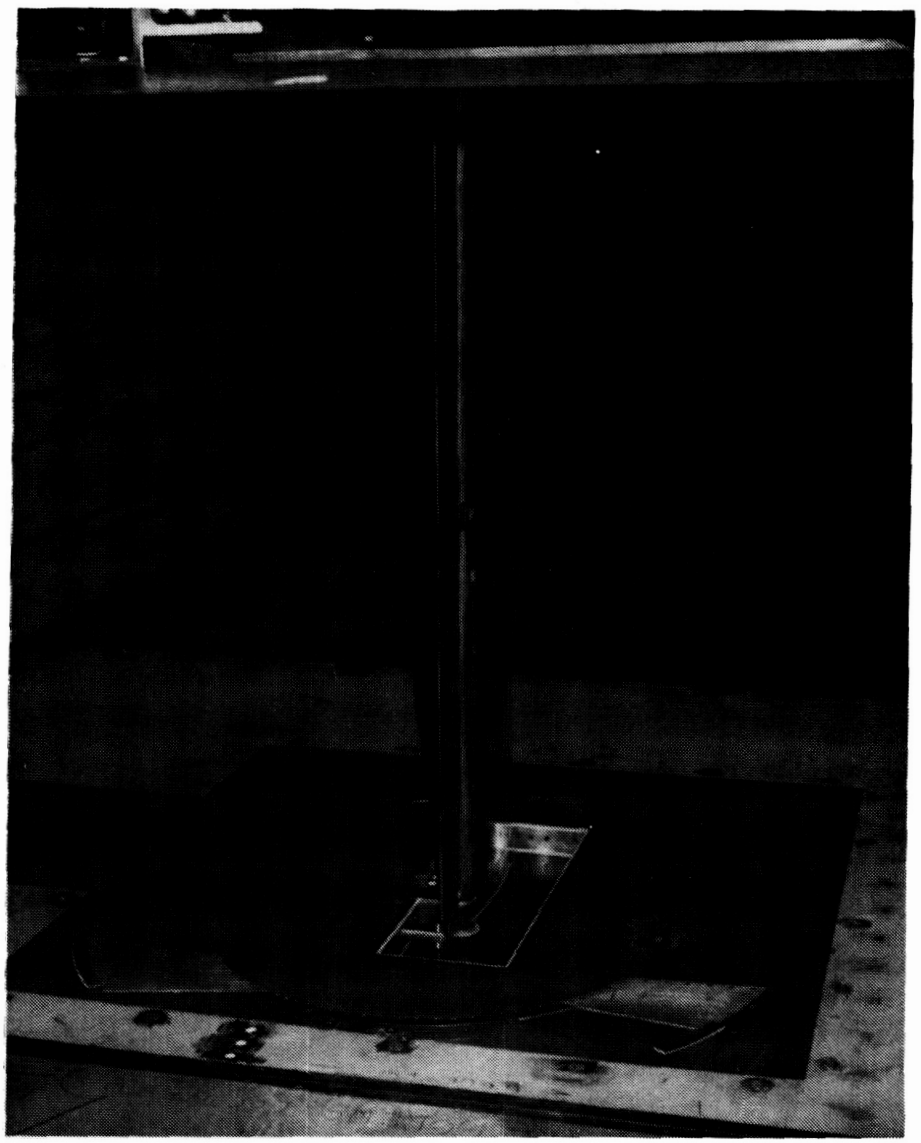

Figure 11.- Upper rear view of oscillating-flap model.

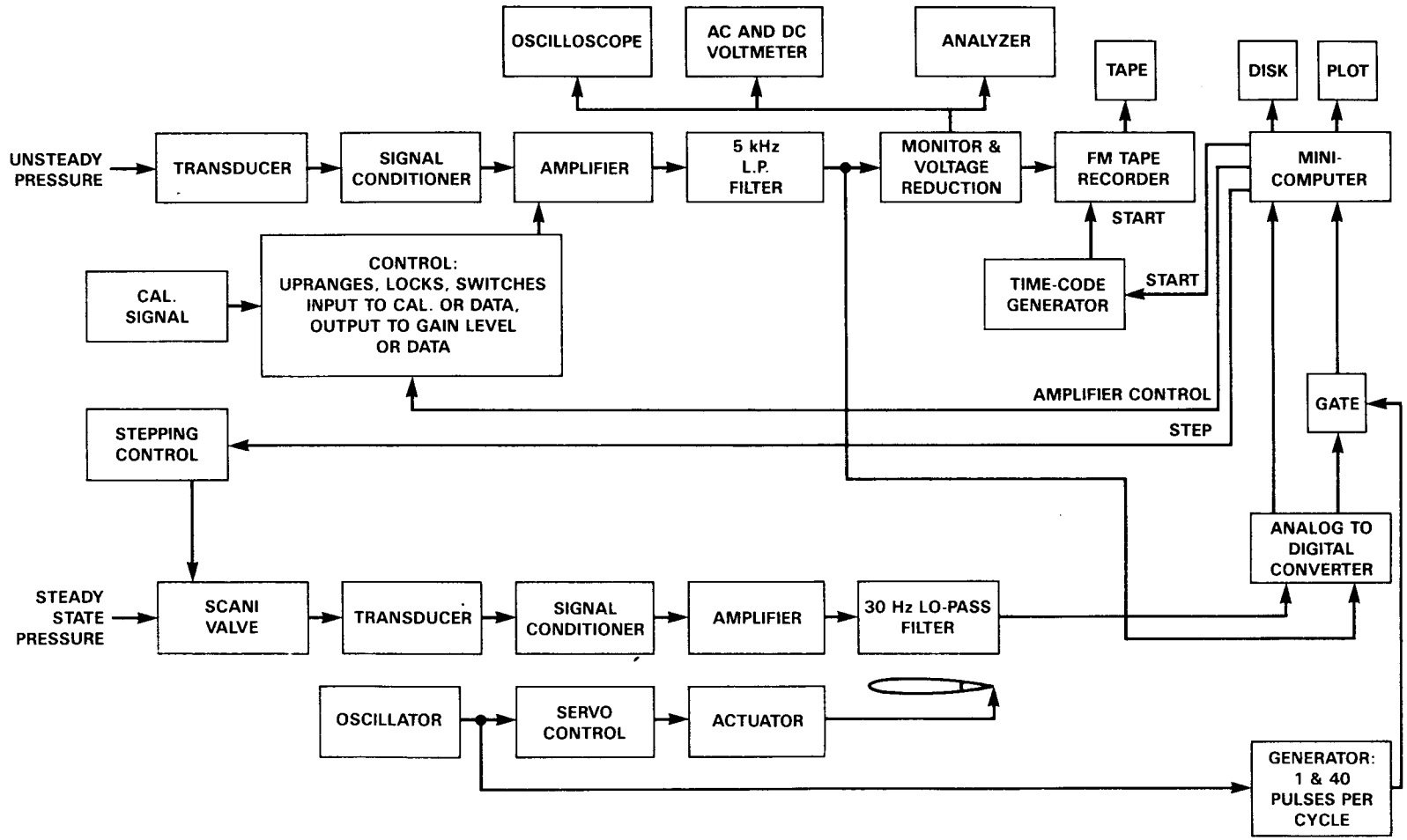

Figure 12.- Typical channel in data-acquisition system.

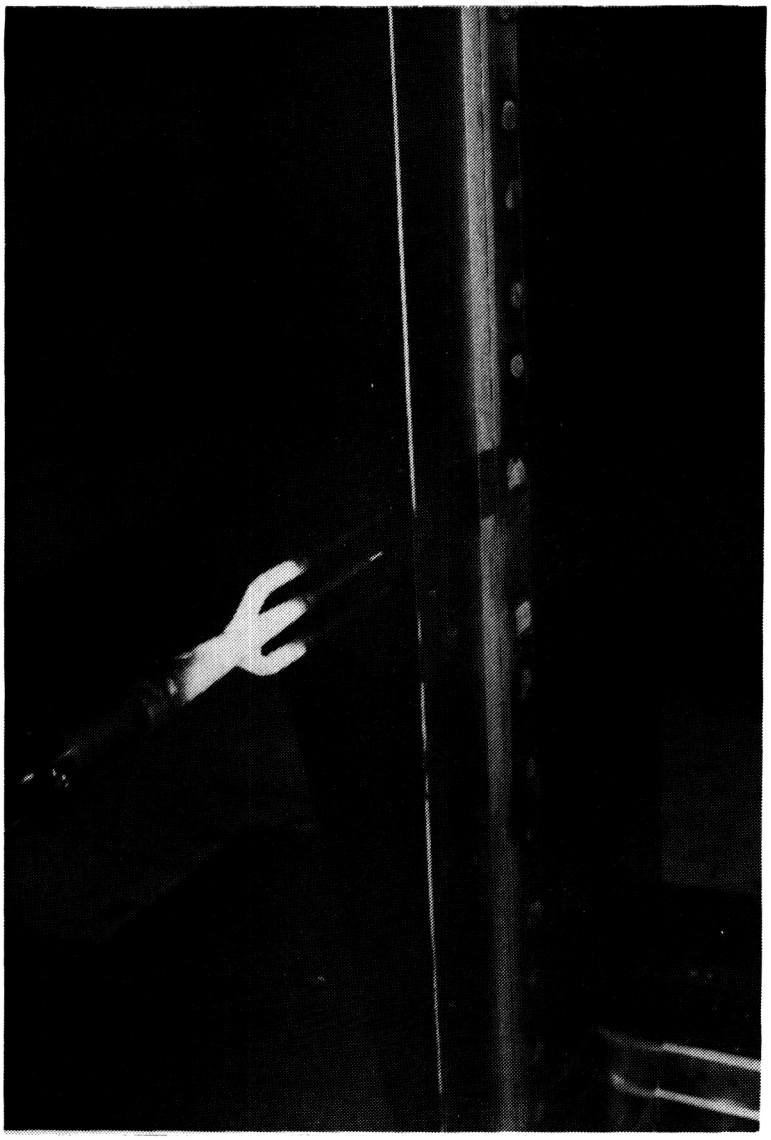

Figure 13.- Wake probe.

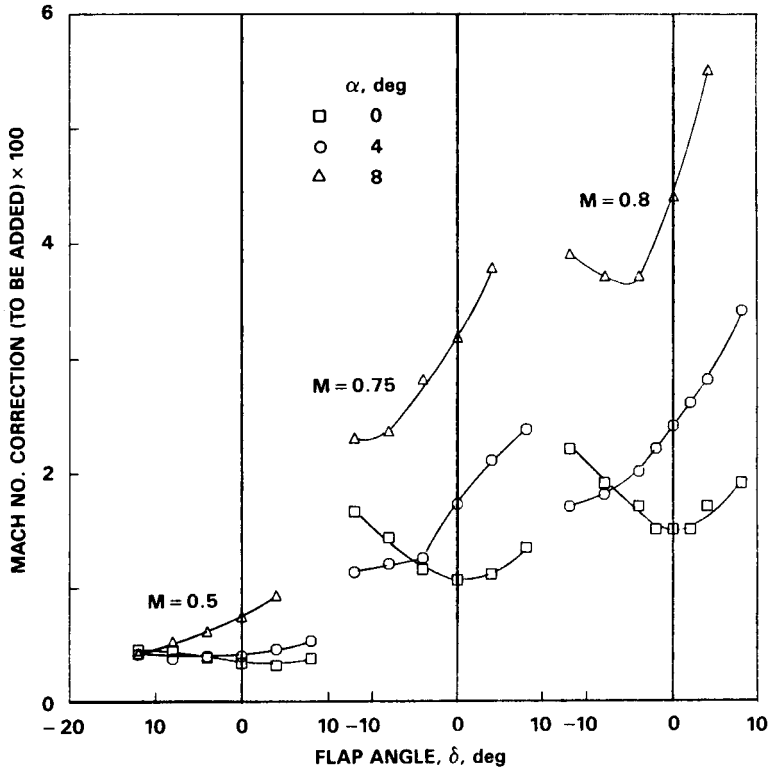

Figure 14.- Mach number corrections from measured floor and ceiling pressures by the method in reference 8.

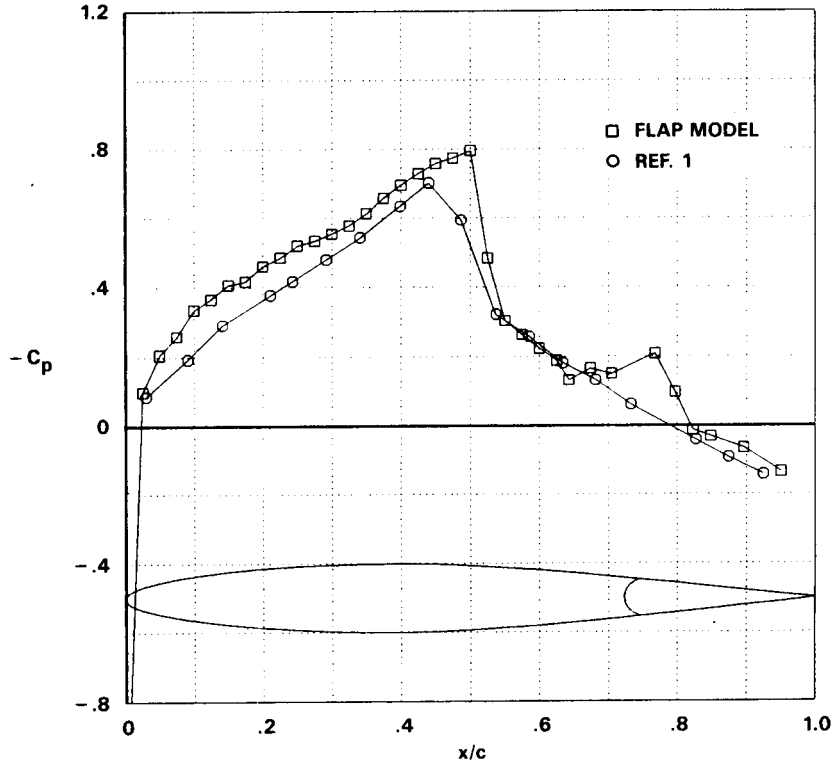

Figure 15.- A comparison of upper-surface pressure; M = 0.8, RN = 13 million, x = 0, δ = 0.

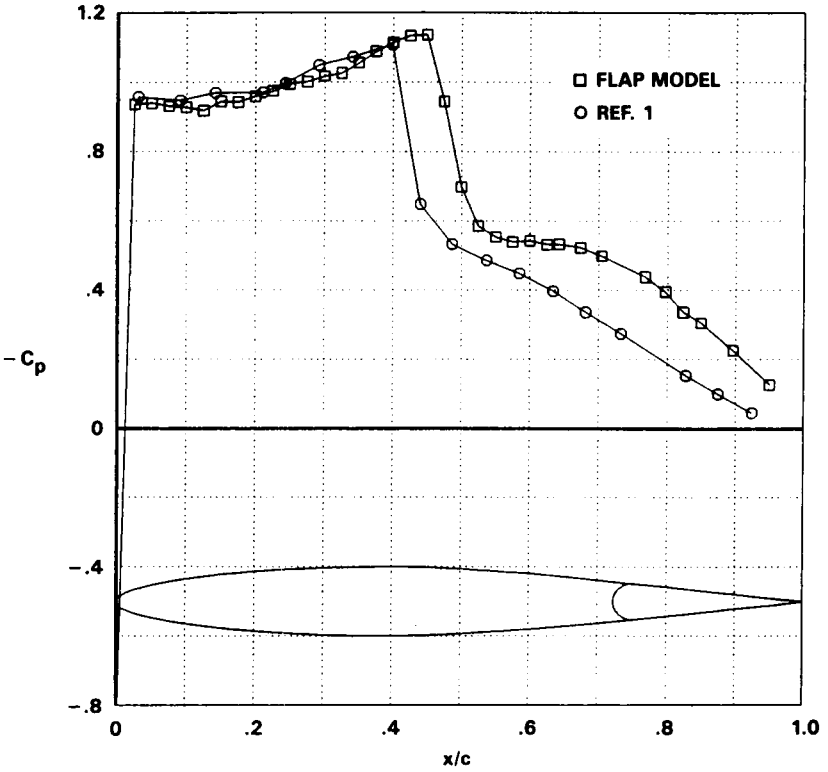

Figure 16.- A comparison of upper-surface pressures; M = 0.8, RN = 12 million, $\alpha = 4°$, $\delta = 0$.

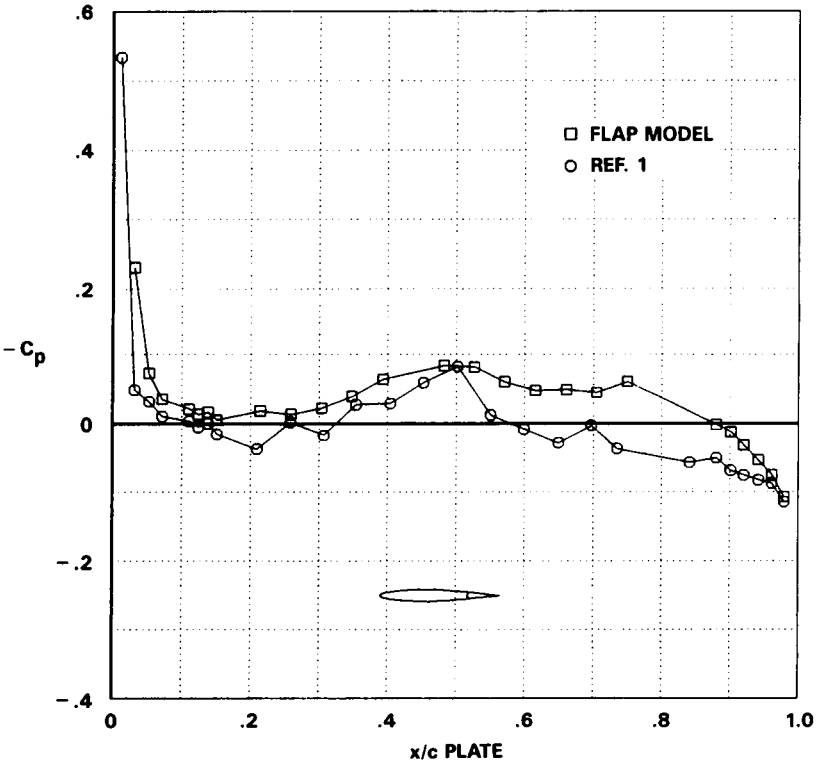

Figure 17.- A comparison of pressures on the inner splitter-plate surface 1.1 to 1.5 chord lengths above the airfoil; M = 0.80, RN = 13 million, $\alpha = 0$, $\delta = 0$.

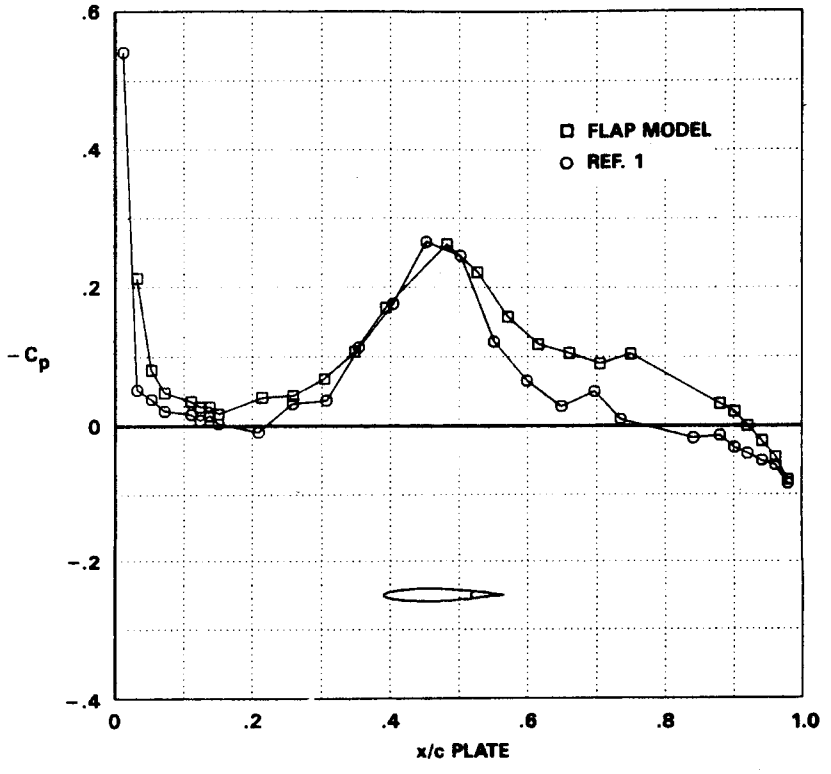

Figure 18.- A comparison of pressures on the inner splitter-plate surface 1.1 to 1.5 chord lengths above the airfoil; M = 0.80, RN = 12 million, α = 4°, δ = 0.

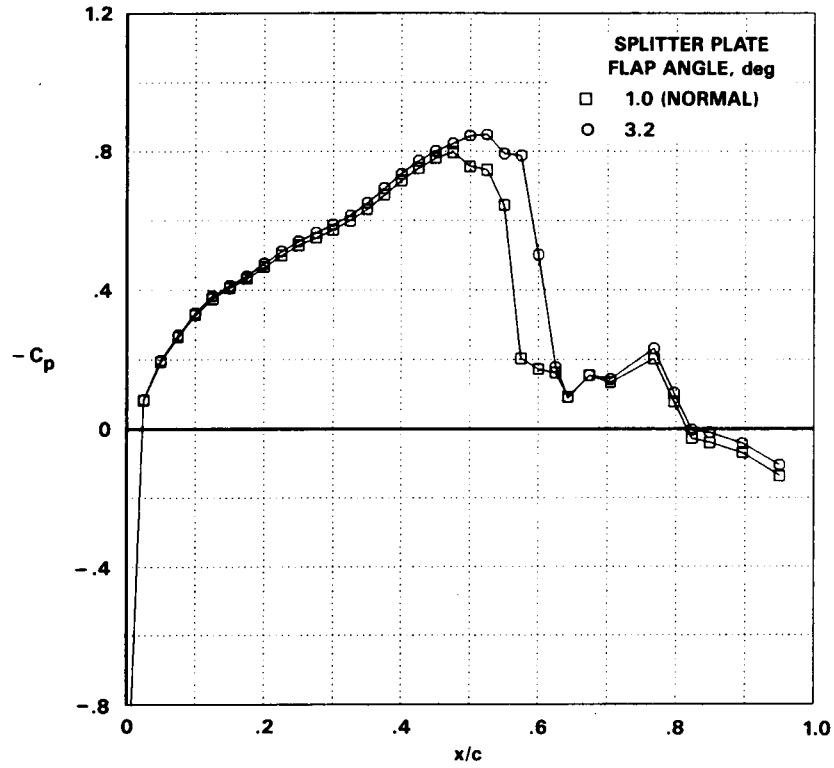

Figure 19.- A comparison of upper-surface pressures with different splitter-plate flap deflections; M = 0.80, RN = 6.5 million, α = 0, δ = 0.

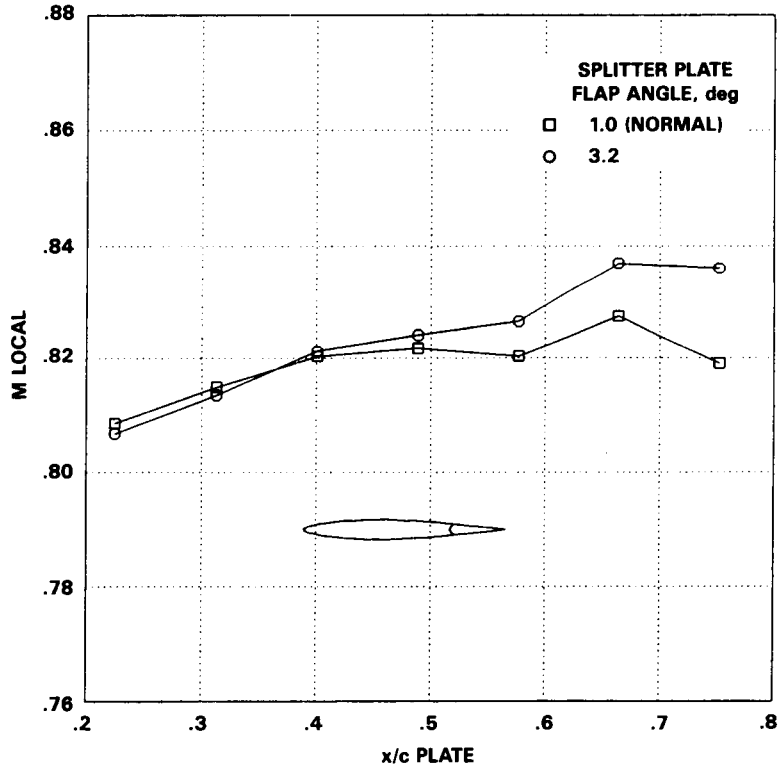

e 20.- A comparison of local Mach numbers on the ceiling for different litter-plate flap deflections; M = 0.80, RN = 6.5 million, α = 0, δ = 0.

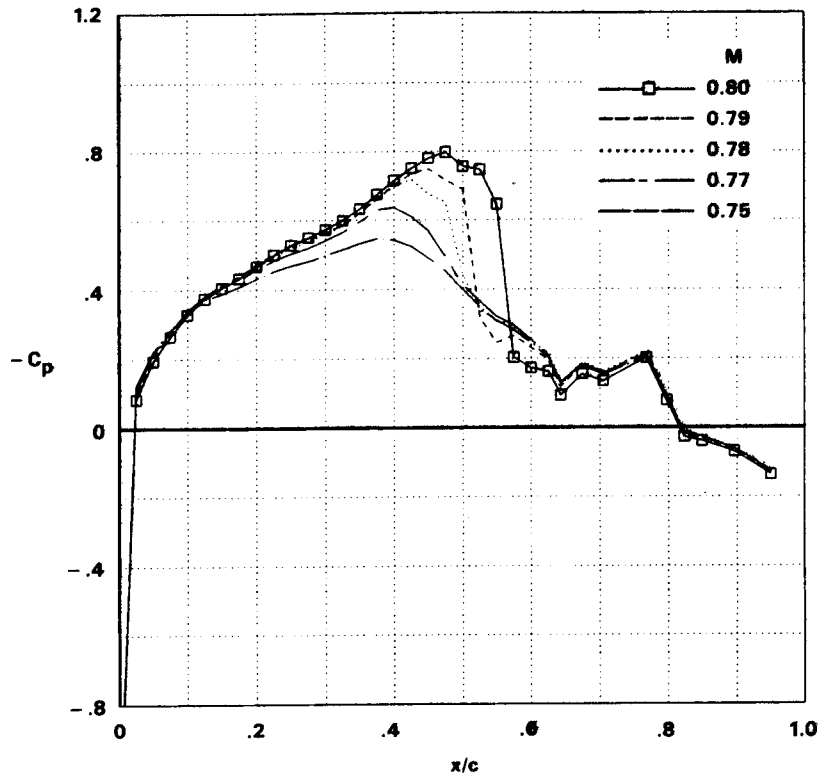

Figure 21.- The effect of Mach number on upper-surface pressures; RN = 6.5 million, $\alpha = 0$, $\delta = 0$.

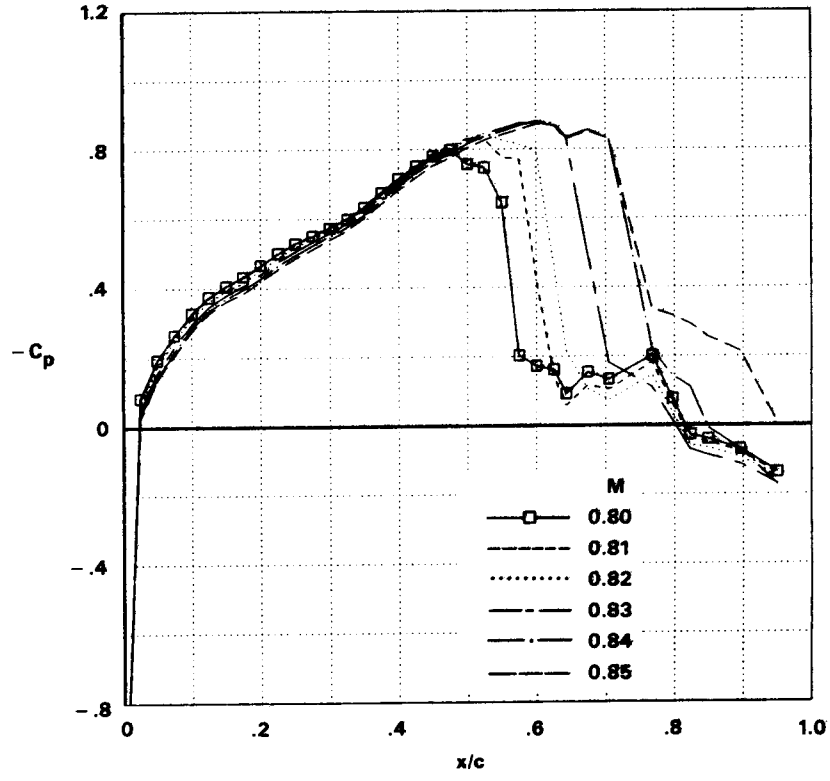

Figure 22.- The effect of Mach number on upper-surface pressures; RN = 6.5 million, $\alpha = 0$, $\delta = 0$.

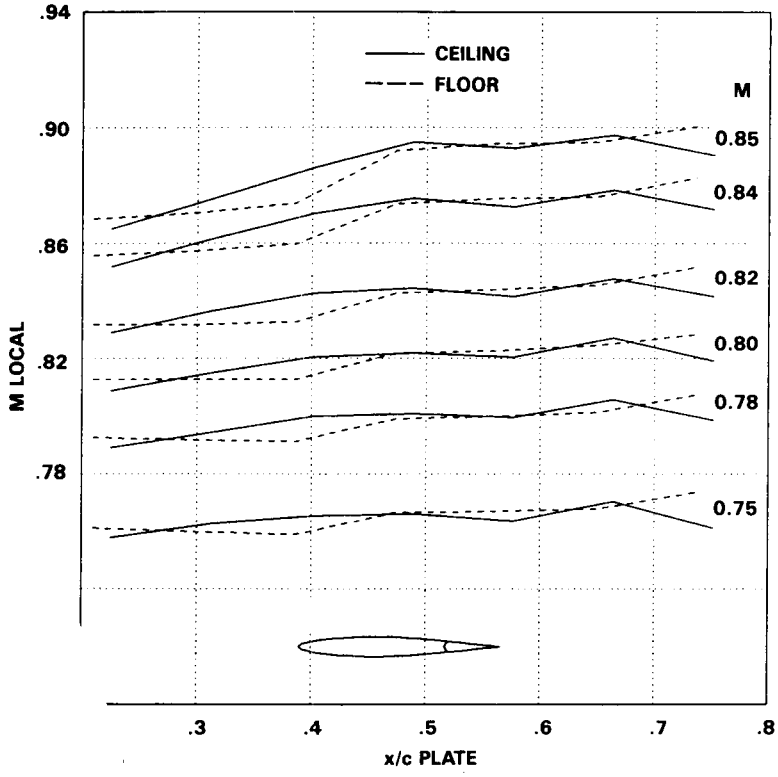

Figure 23. .ect of Mach number on the local Mach number distribution o iling and floor; RN = 6.5 million, α = 0, δ = 0.

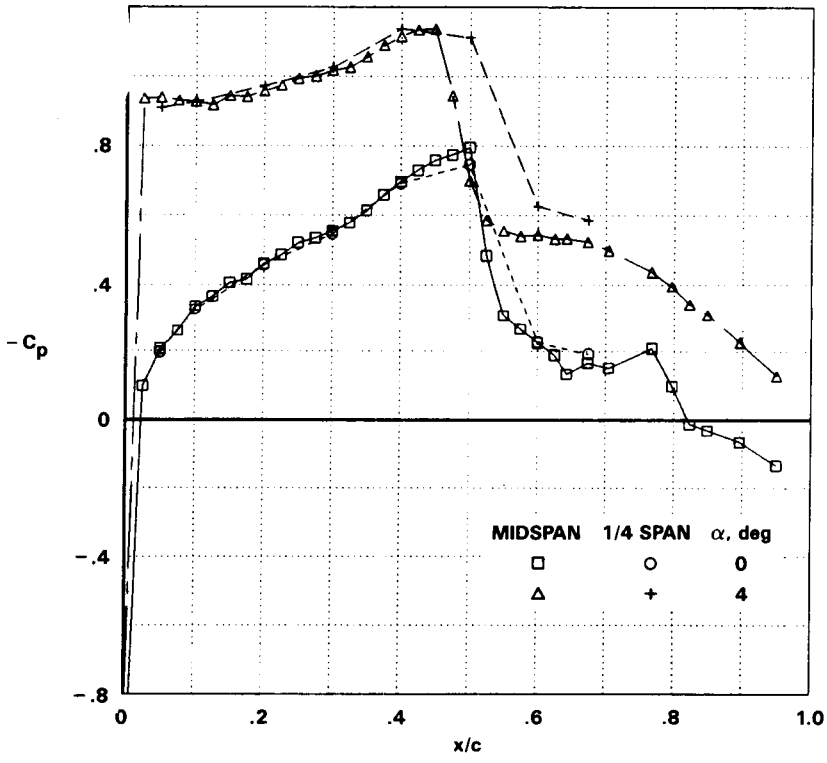

Figure 24.- Upper-surface pressures at two spanwise locations and angles of attack; M = 0.80, RN = 12.5 to 12.9 million, δ = 0.

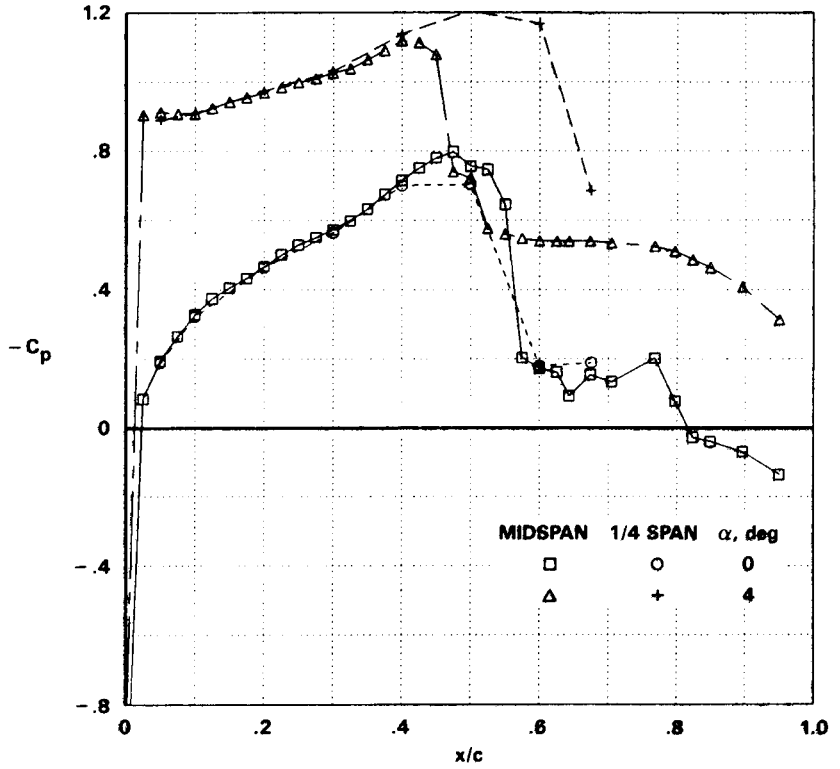

Figure 25.- Upper-surface pressures at two spanwise locations and angles of attack; M = 0.80, RN = 6.5 million, δ = 0.

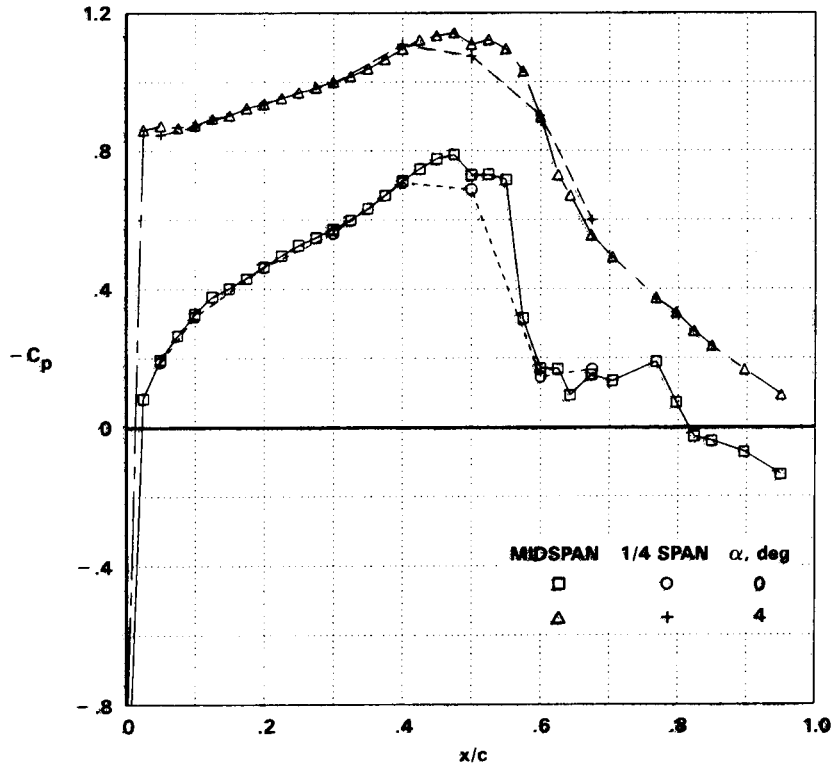

Figure 26.- Upper-surface pressures at two spanwise locations and angles of attack; M = 0.80, RN = 3.4 million, δ = 0.

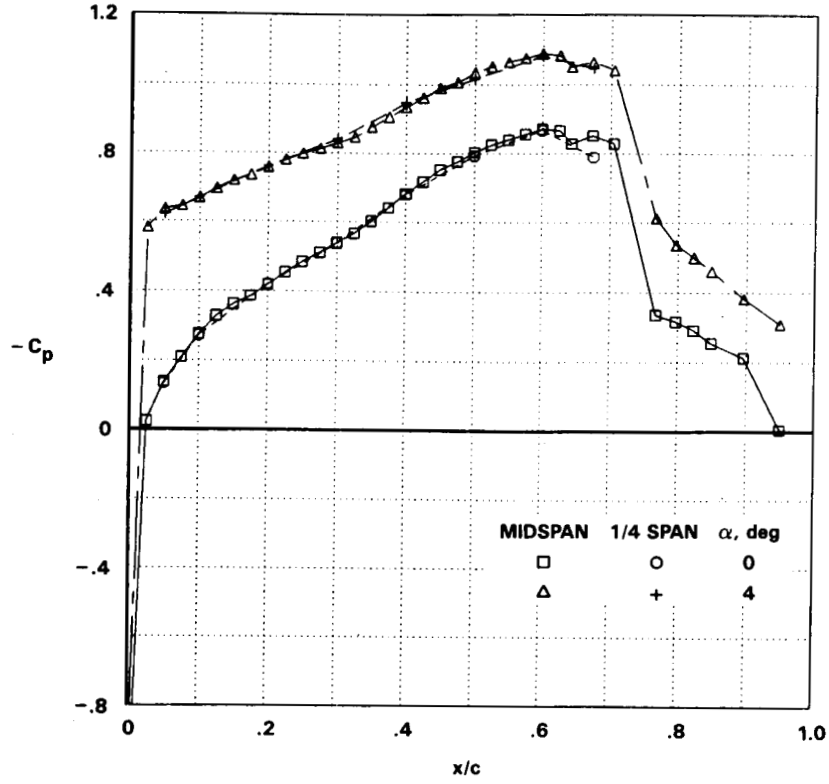

Figure 27.- Upper-surface pressures at two spanwise locations and angles of attack; M = 0.85, RN ≈ 6.5 million, δ = 0.

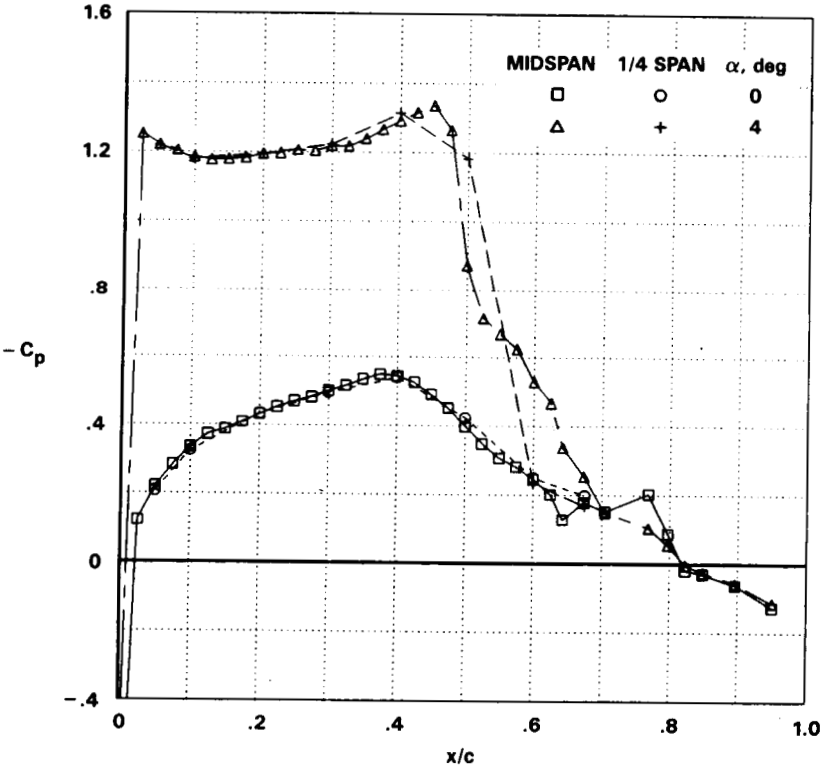

Figure 28.- Upper-surface pressures at two spanwise locations and angles of attack; M = 0.75, RN = 6.3 million, δ = 0.

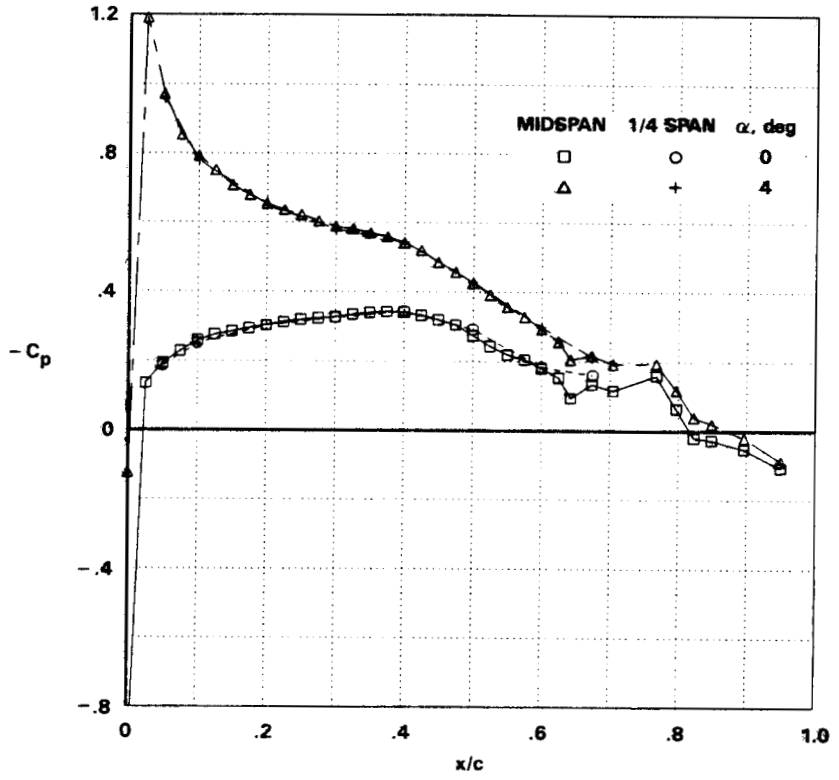

Figure 29.- Upper-surface pressures at two spanwise locations and angles of attack; M = 0.50, RN ≈ 5.0 million, δ = 0.

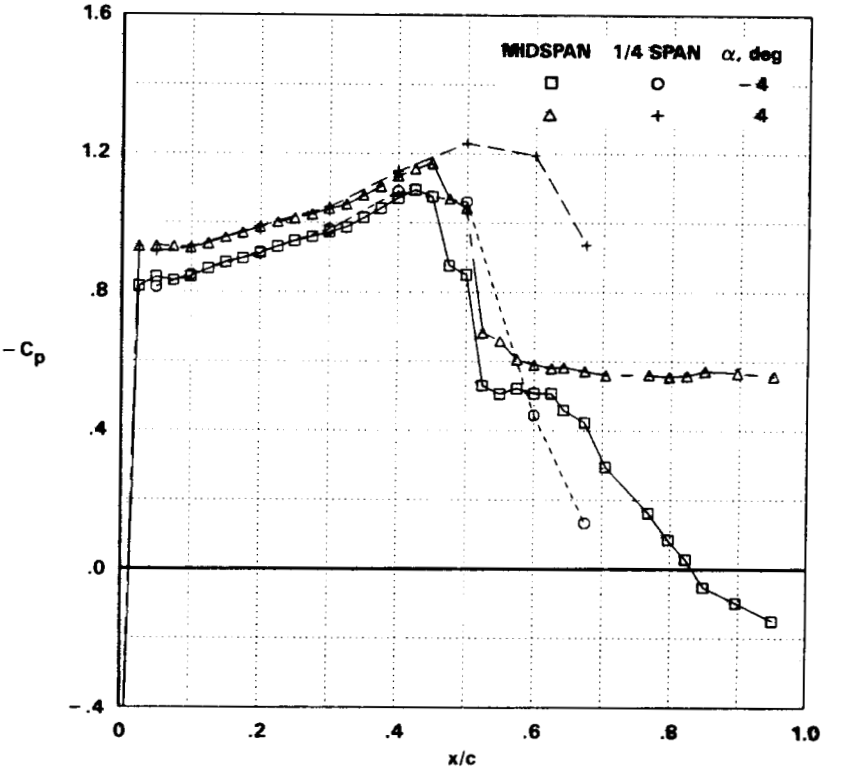

Figure 30.- Upper-surface pressures at two spanwise locations and flap angles; M = 0.80, RN = 6.4 million, α = 4°.

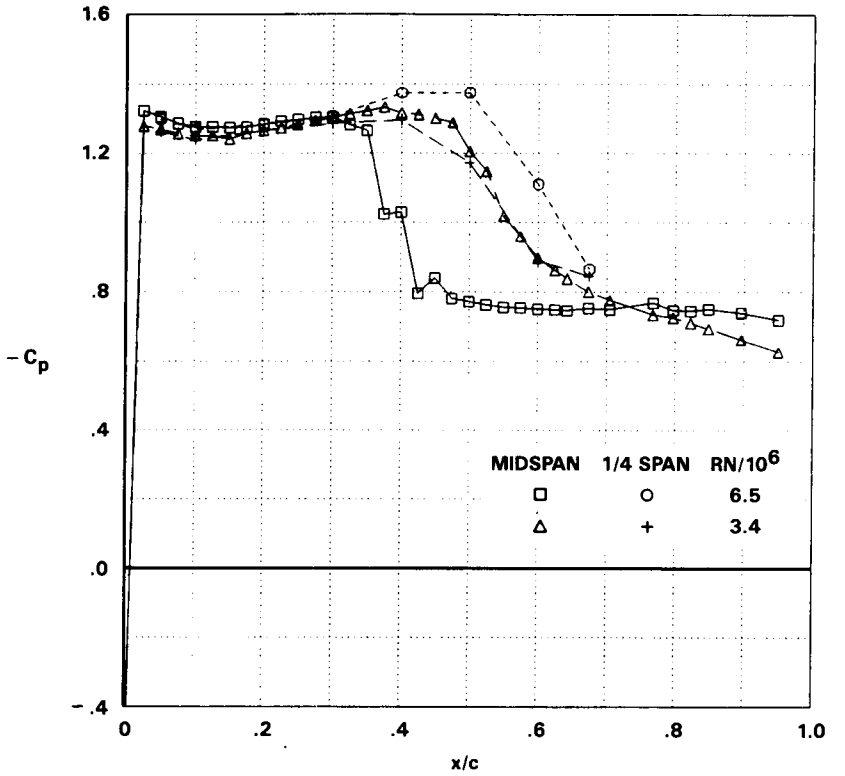

Figure 31.- Upper-surface pressures at two spanwise stations and Reynolds numbers; M = 0.80, α = 8°, δ = 0.

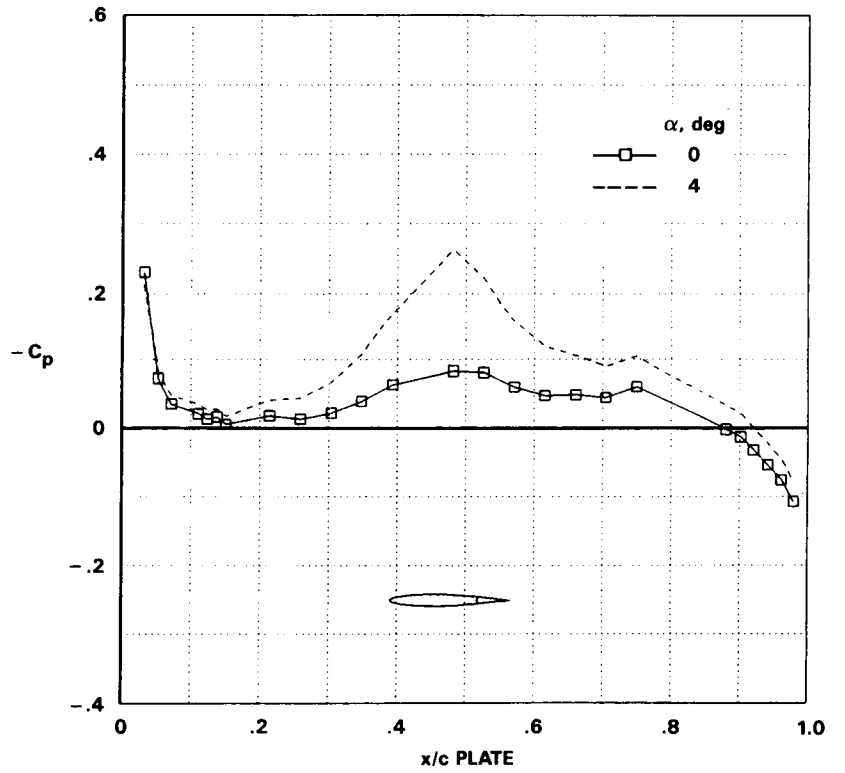

Figure 32.- Pressures on the inside surface of the splitter plate 1.2 to 1.5 chord lengths above the airfoil; M = 0.80, RN = 12.5 to 12.9 million, δ = 0.

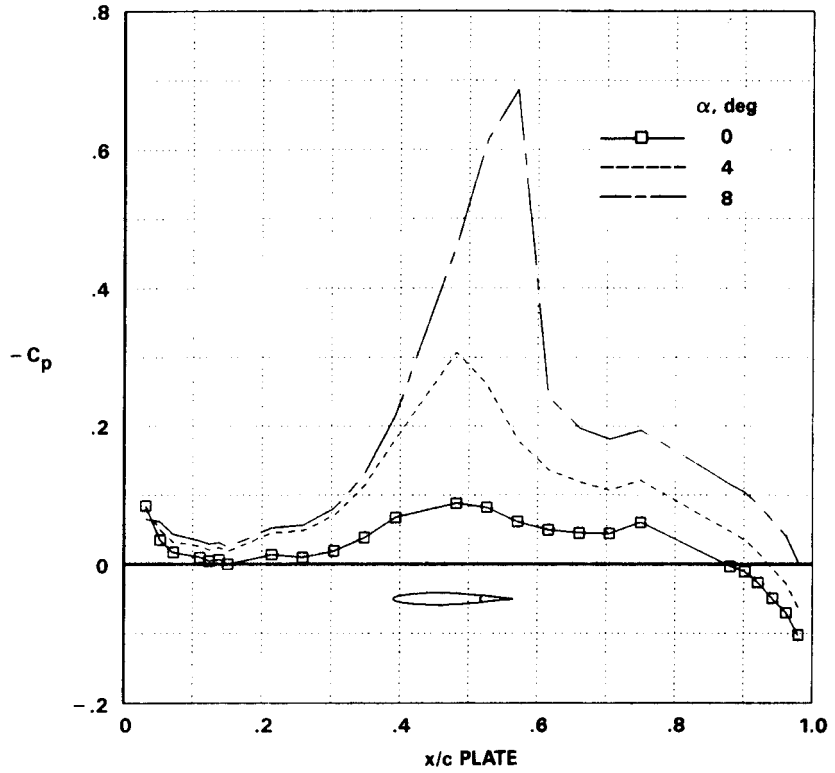

Figure 33.- Pressures on the inside surface of the splitter plate 1.2 to 1.5 chord lengths above the airfoil; M = 0.80, RN ≈ 6.5 million, δ = 0.

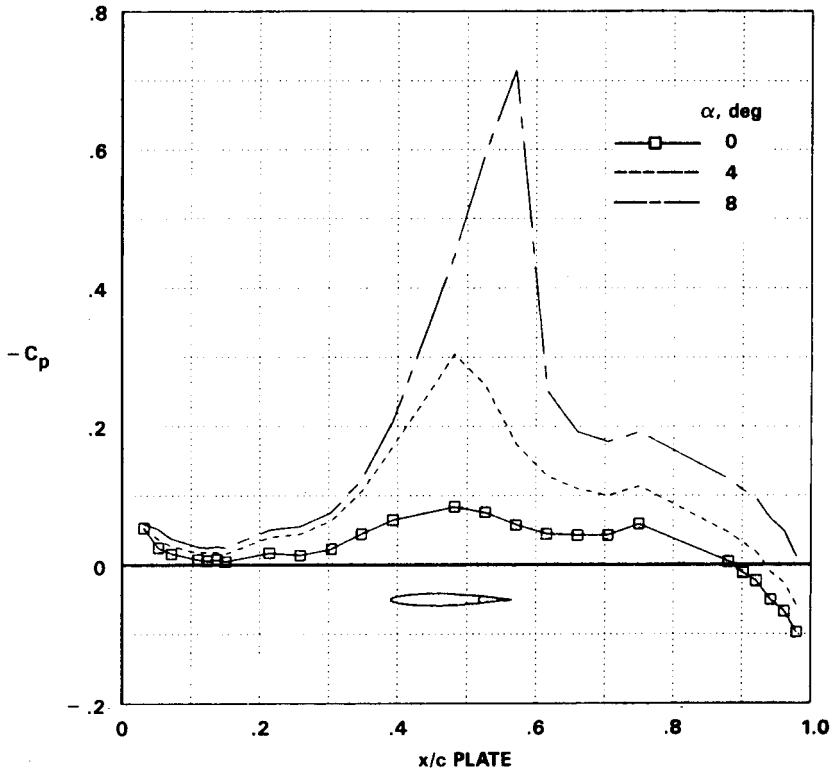

Figure 34.- Pressures on the inside surface of the splitter plate 1.2 to 1.5 chord lengths above the airfoil; M = 0.80, RN = 3.4 million, δ = 0.

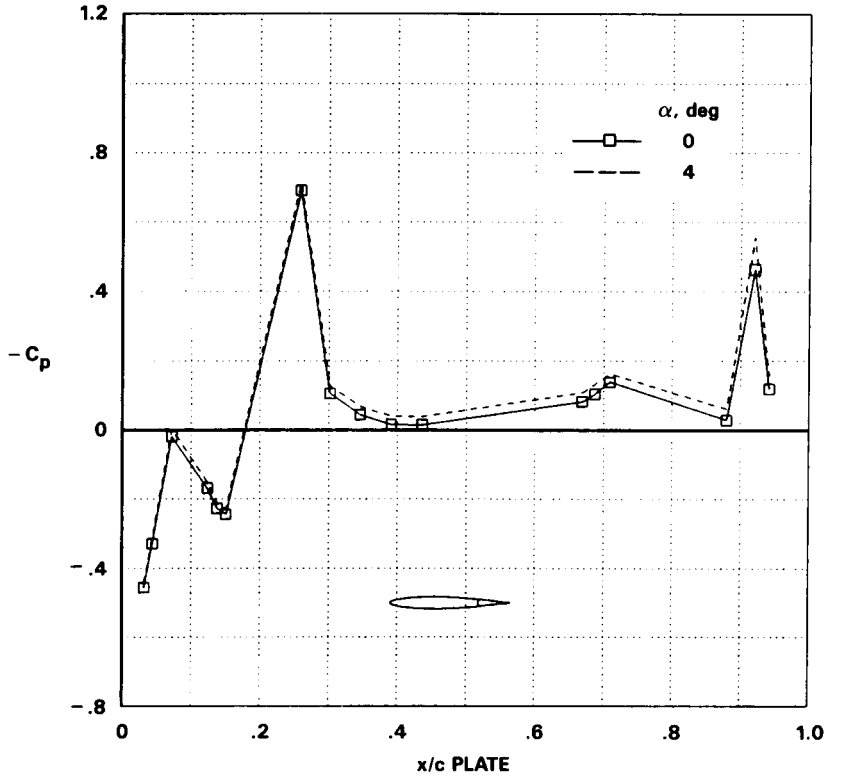

Figure 35.- Pressures on the outside surface of the splitter plate; M = 0.80, RN = 12.5 to 12.9 million, δ = 0.

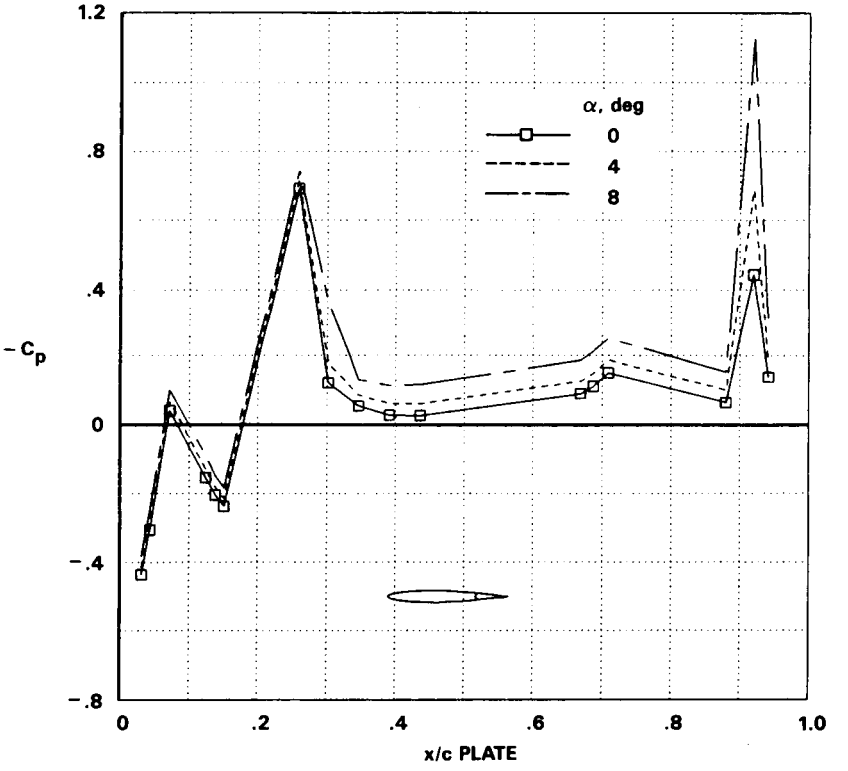

Figure 36.- Pressures on the outside surface of the splitter plate; M = 0.80, RN ≈ 6.5 million, δ = 0.

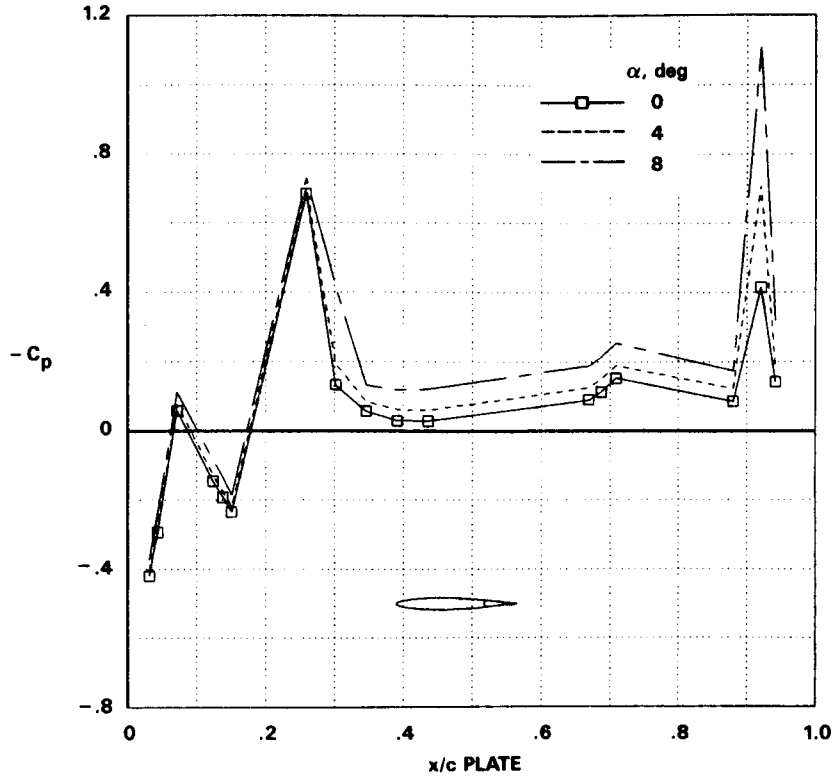

Figure 37.- Pressures on the outside surface of the splitter plate; M = 0.80, RN = 3.4 million, δ = 0.

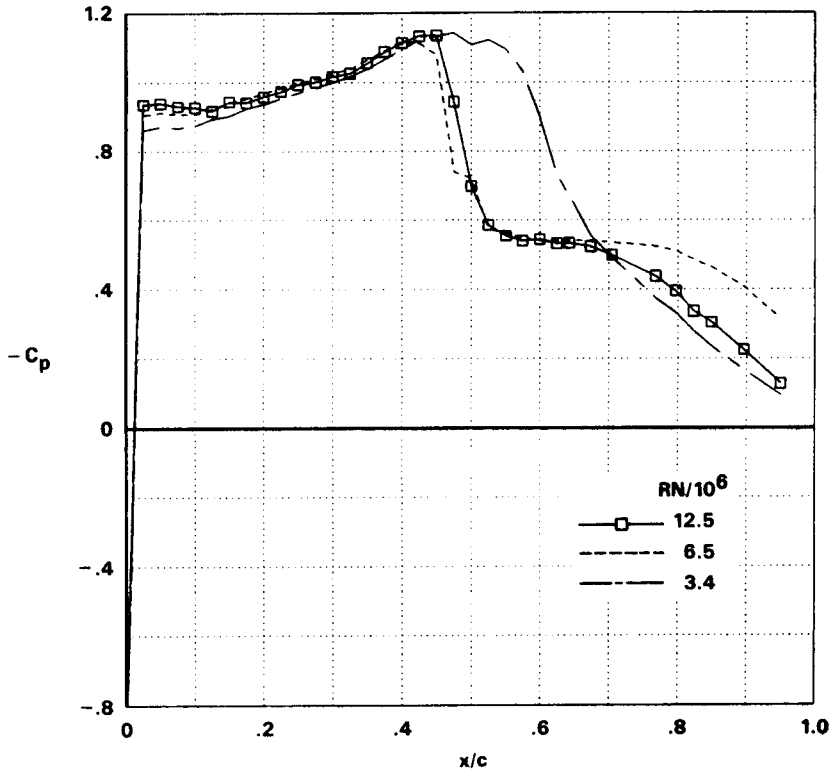

Figure 38.- The effect of Reynolds number on the pressure distribution; M = 0.80, α = 4°, δ = 0.

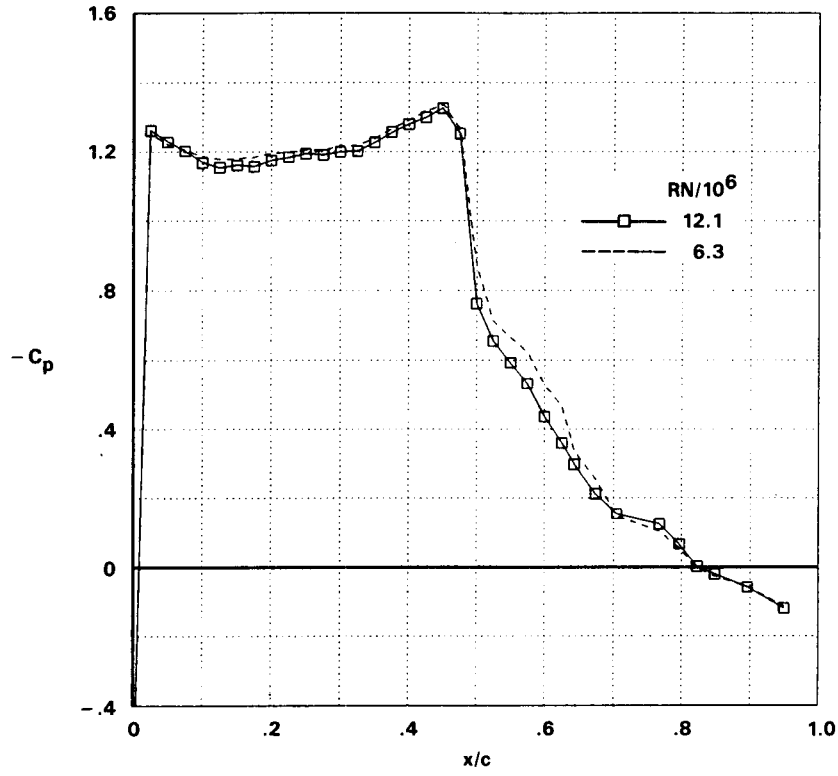

Figure 39.- The effect of Reynolds number on the pressure distribution; M = 0.75, α = 4°, δ = 0.

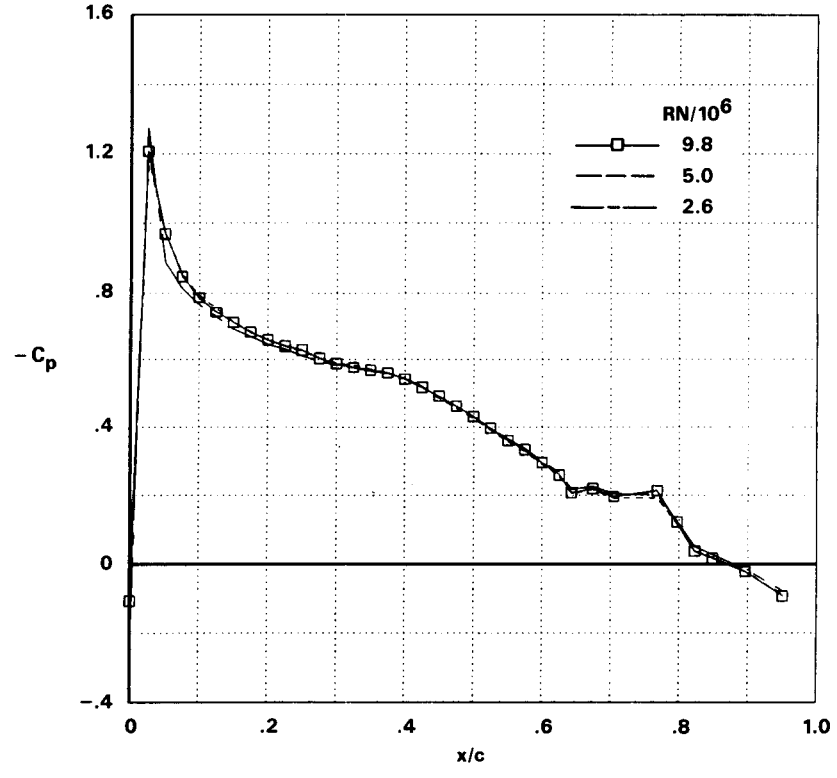

Figure 40.- The effect of Reynolds number on the pressure distribution; M = 0.50, α = 4°, δ = 0.

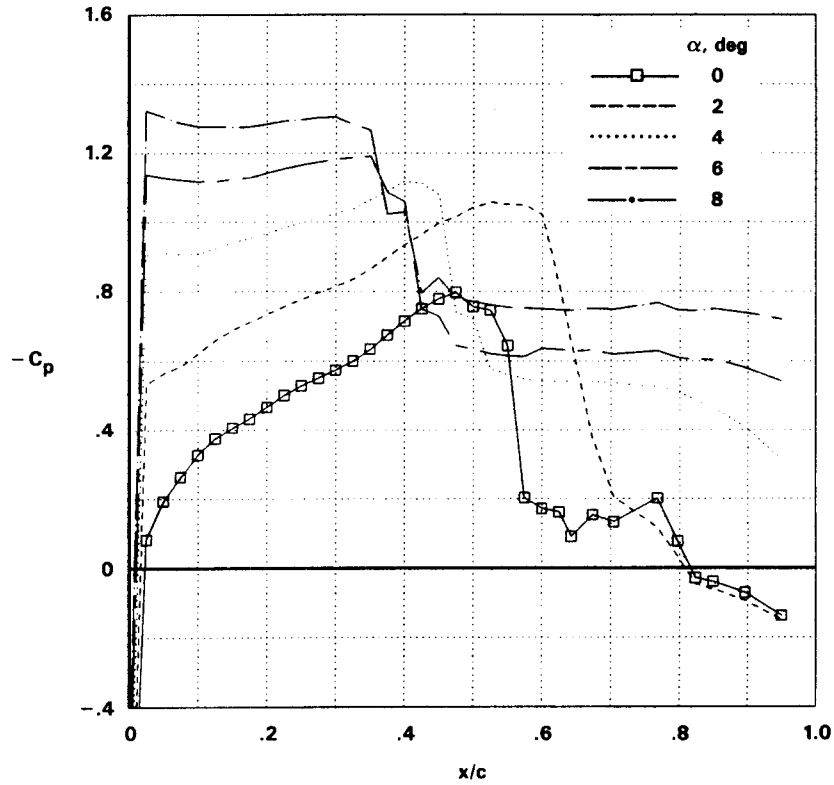

Figure 41.- The effect of angle of attack on the upper-surface pressure distribution; M = 0.80, RN ≈ 6.5 million, δ = 0.

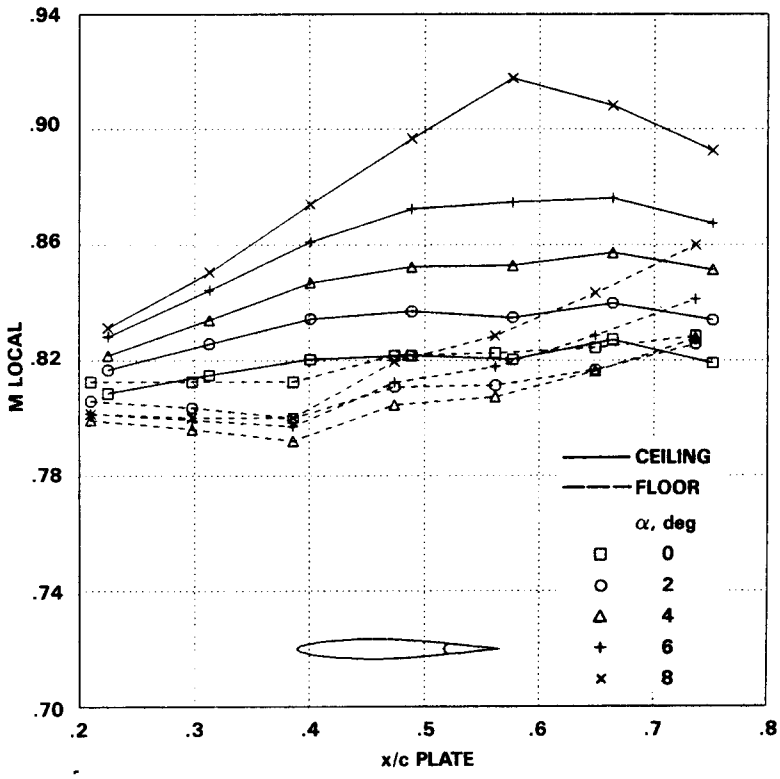

Figure 42.- The effect of angle of attack on the Mach-number distribution on the ceiling and floor; M = 0.80, RN ≈ 6.5 million, δ = 0.

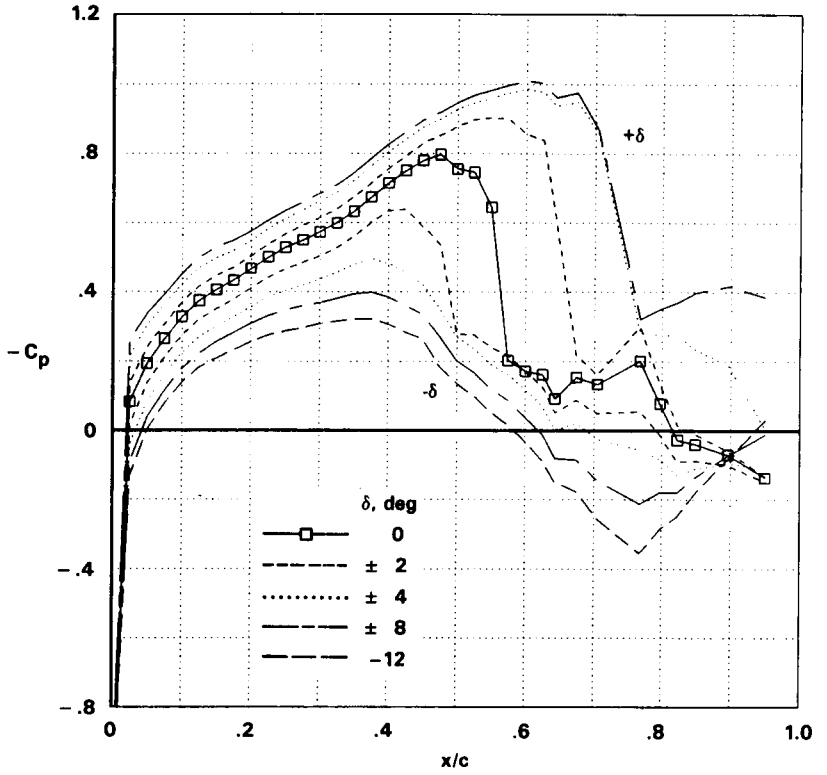

Figure 43.- The effect of flap angle on the upper-surface pressures; M = 0.80, RN ≈ 6.5 million, α = 0.

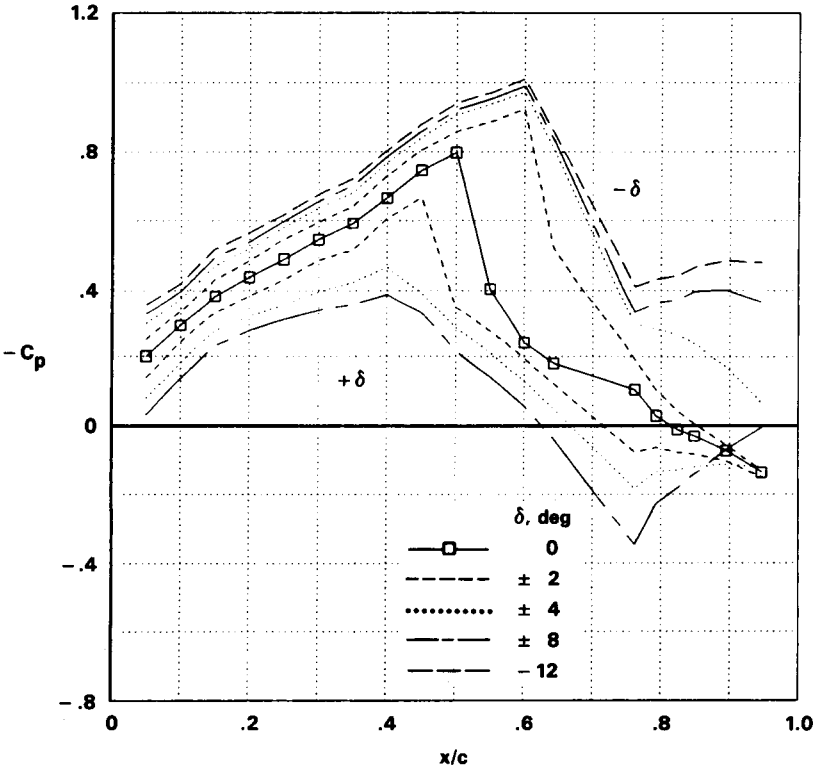

Figure 44.- The effect of flap angle on the lower-surface pressures; M = 0.80, RN ≈ 6.5 million, α = 0.

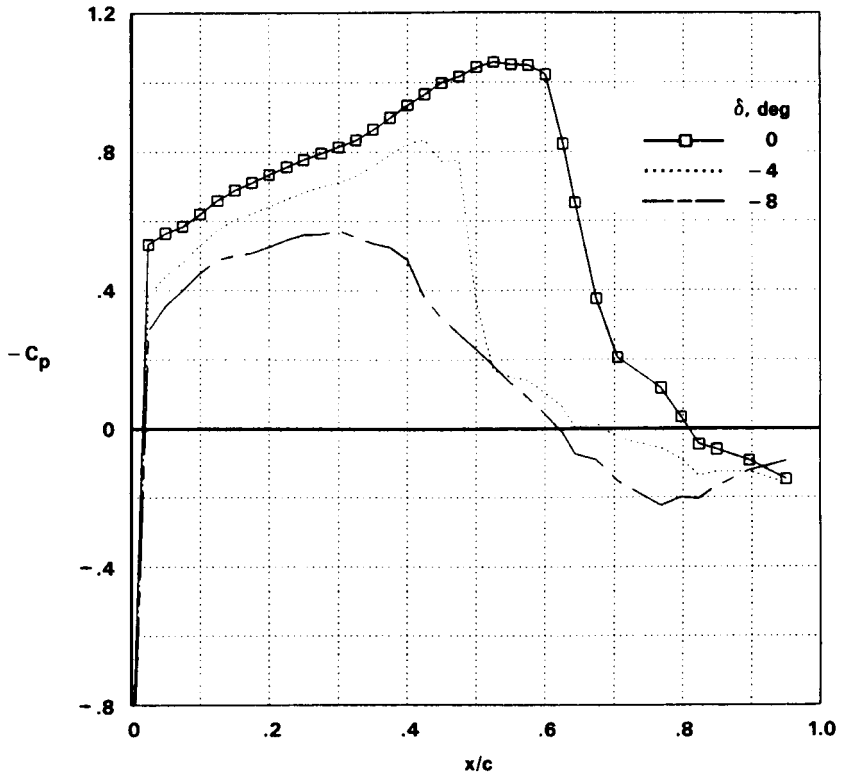

Figure 45.- The effect of flap angle on the upper-surface pressures; M = 0.80, RN ≈ 6.4 million, α = 2°.

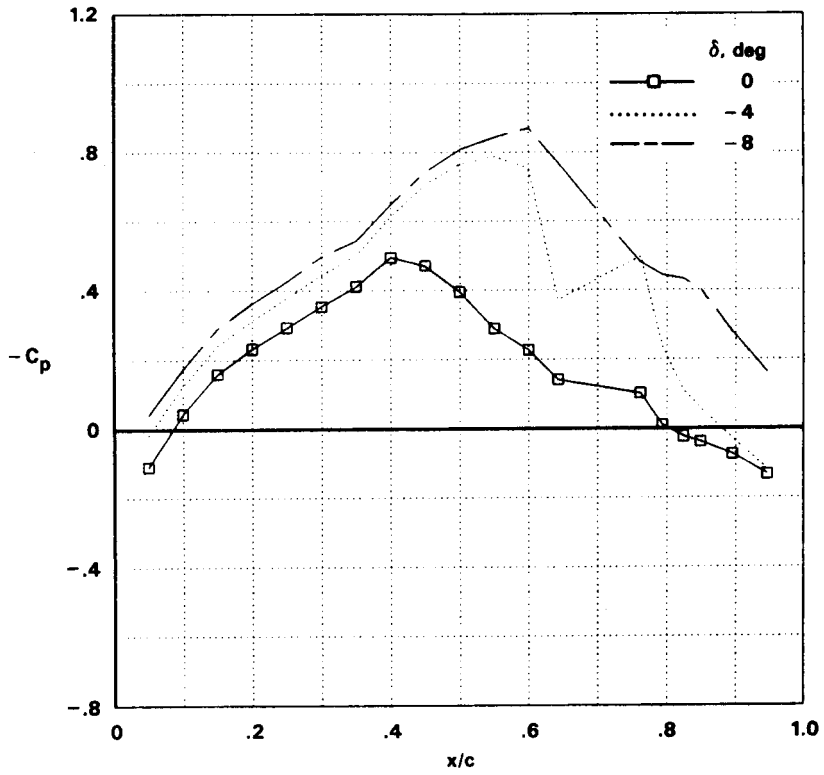

Figure 46.- The effect of flap angle on the lower-surface pressures; M = 0.80, RN ≈ 6.4 million, α = 2°.

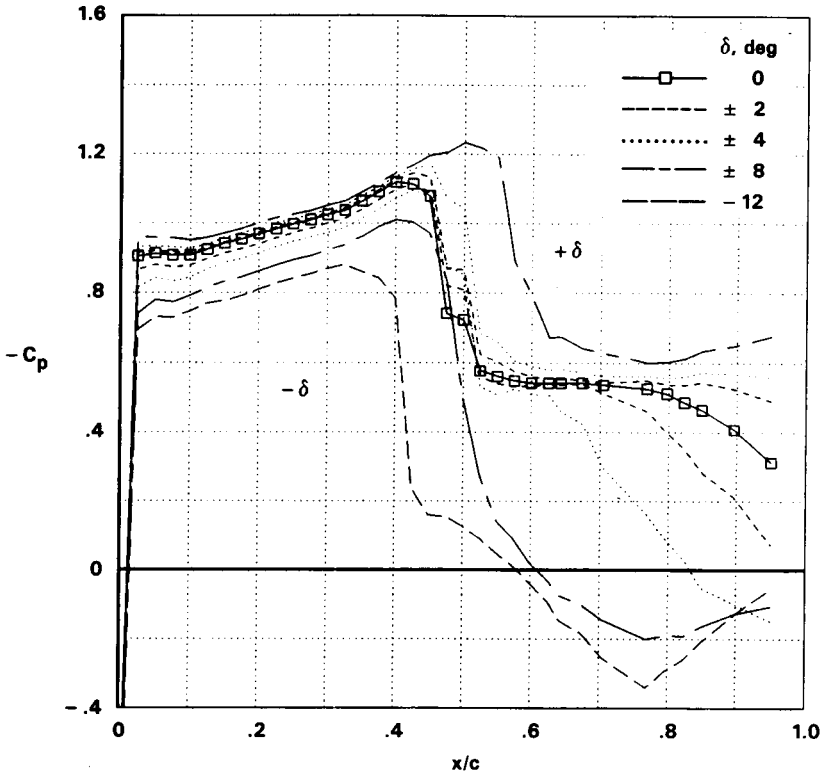

Figure 47.- The effect of flap angle on the upper-surface pressures; M = 0.80, RN = 6.4 million, α = 4°.

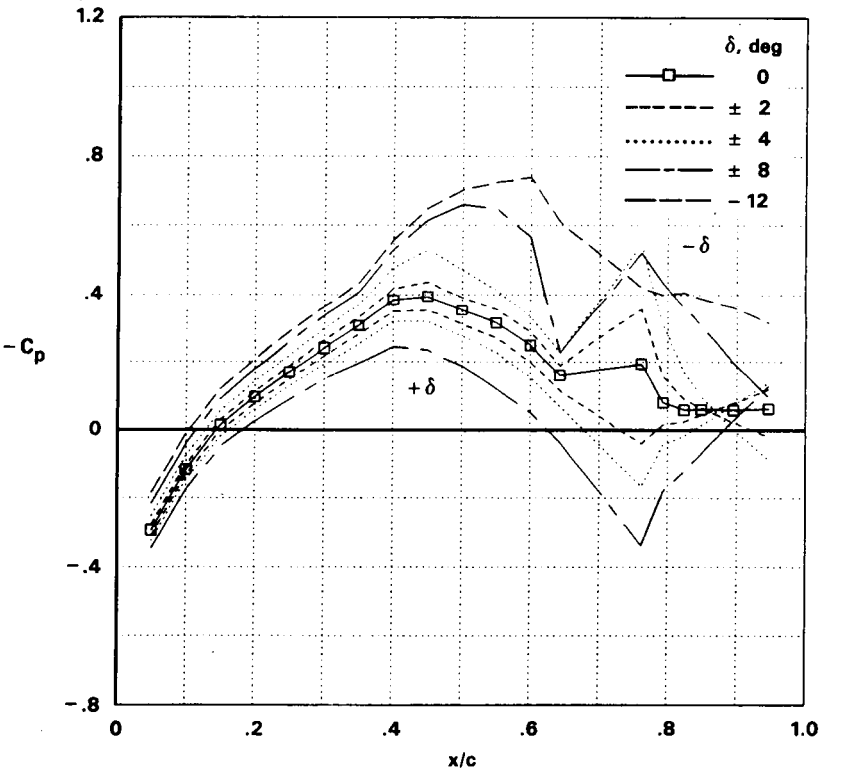

Figure 48.- The effect of flap angle on the lower-surface pressures; M = 0.80, RN = 6.4 million, α = 4°.

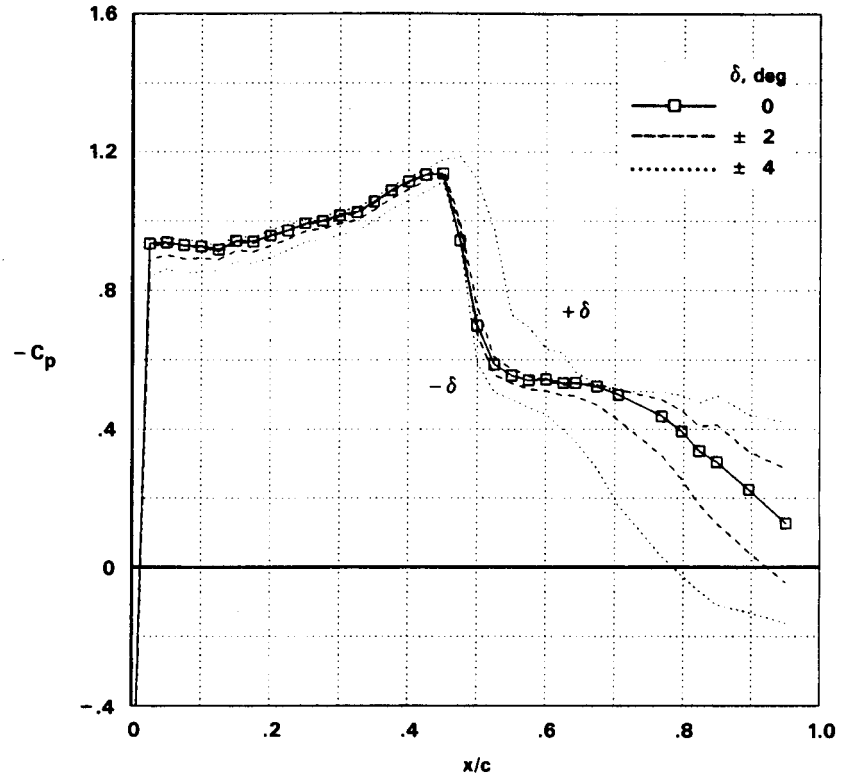

Figure 49.- The effect of flap angle on the upper-surface pressures; M = 0.80, RN ≈ 12.5 million, α = 4°.

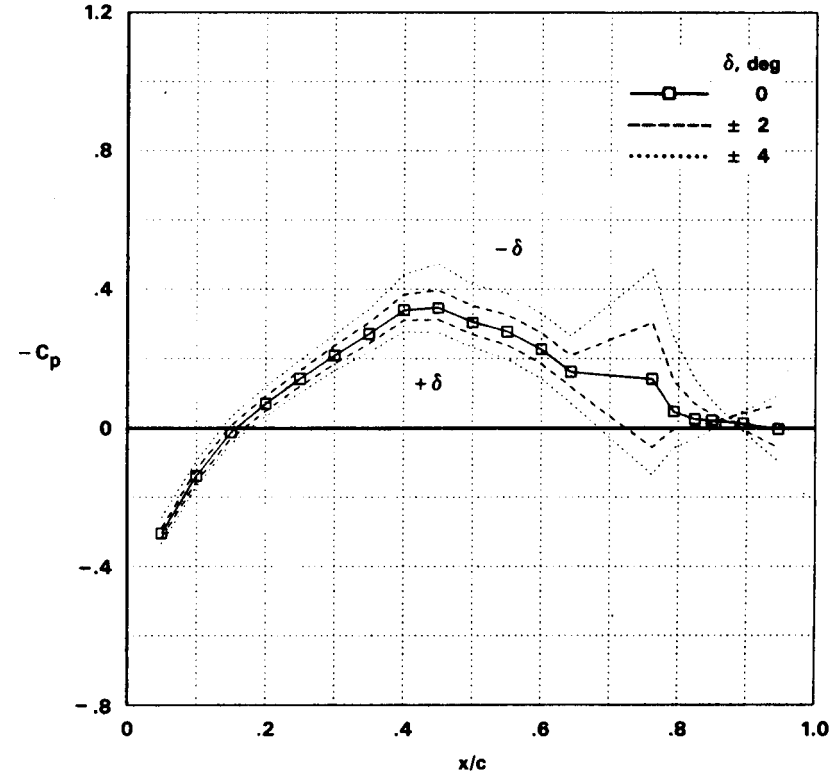

Figure 50.- The effect of flap angle on the lower-surface pressures; M = 0.80, RN ≈ 12.5 million, α = 4.

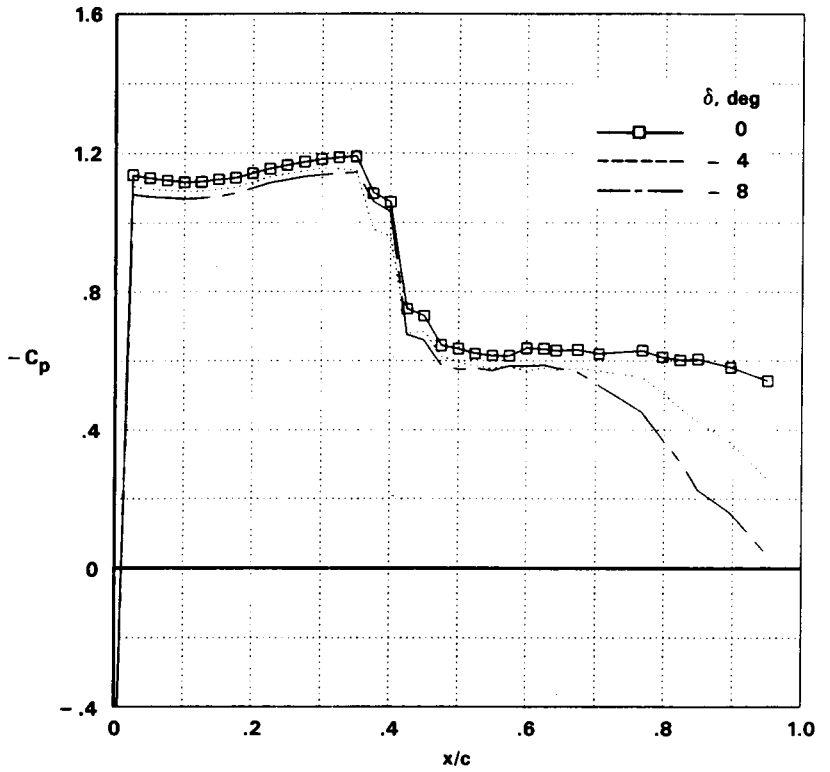

Figure 51.- The effect of flap angle on the upper-surface pressures; M = 0.80, RN ≈ 6.7 million, α = 6°.

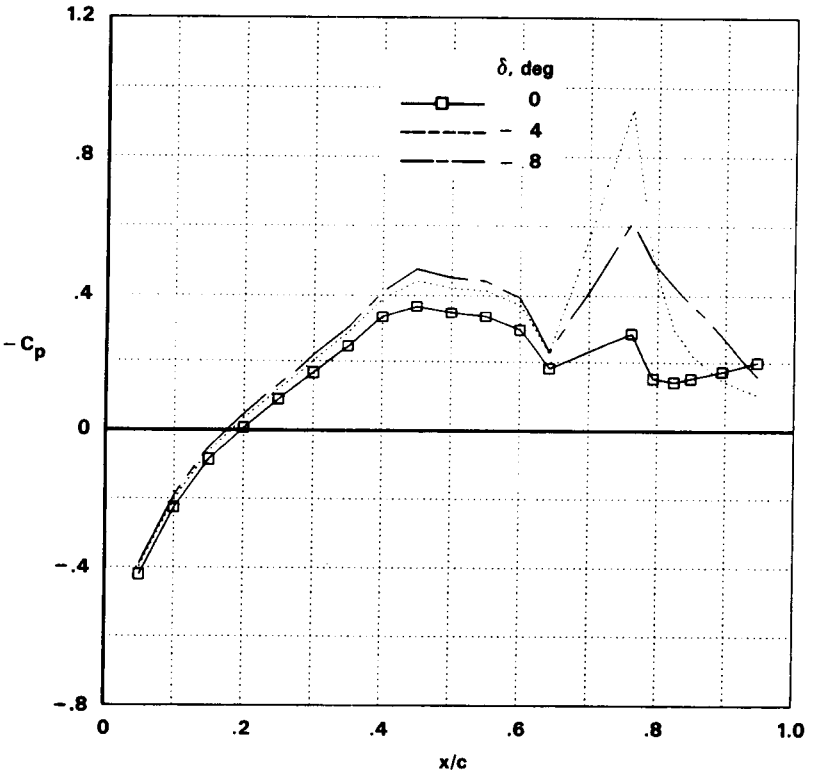

Figure 52.- The effect of flap angle on the lower-surface pressures; M = 0.80, RN ≈ 6.7 million, α = 6°.

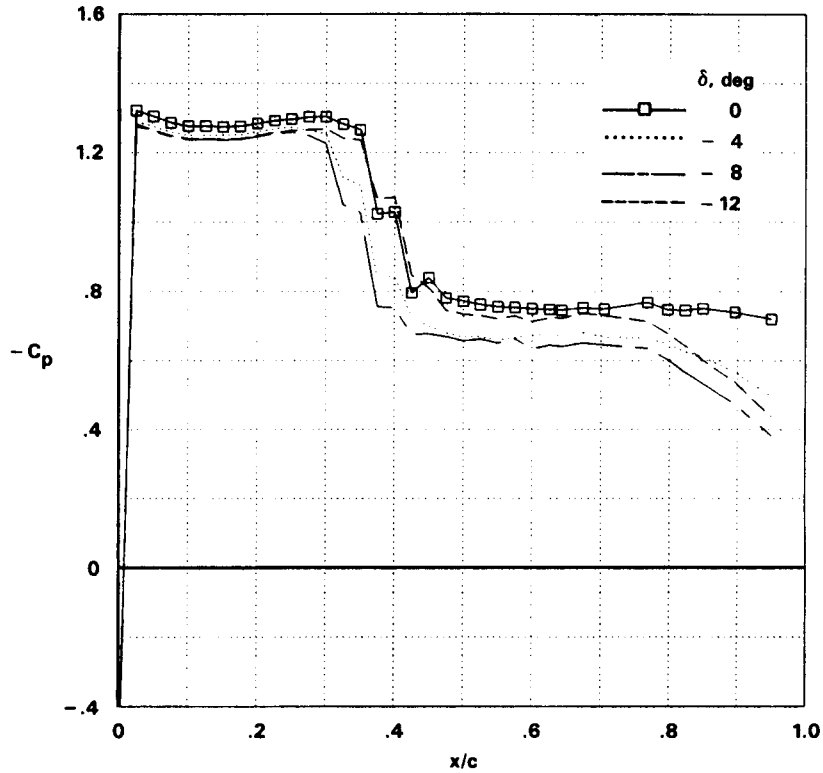

Figure 53.- The effect of flap angle on the upper-surface pressures; M = 0.80, RN = 6.5 million, α = 8°.

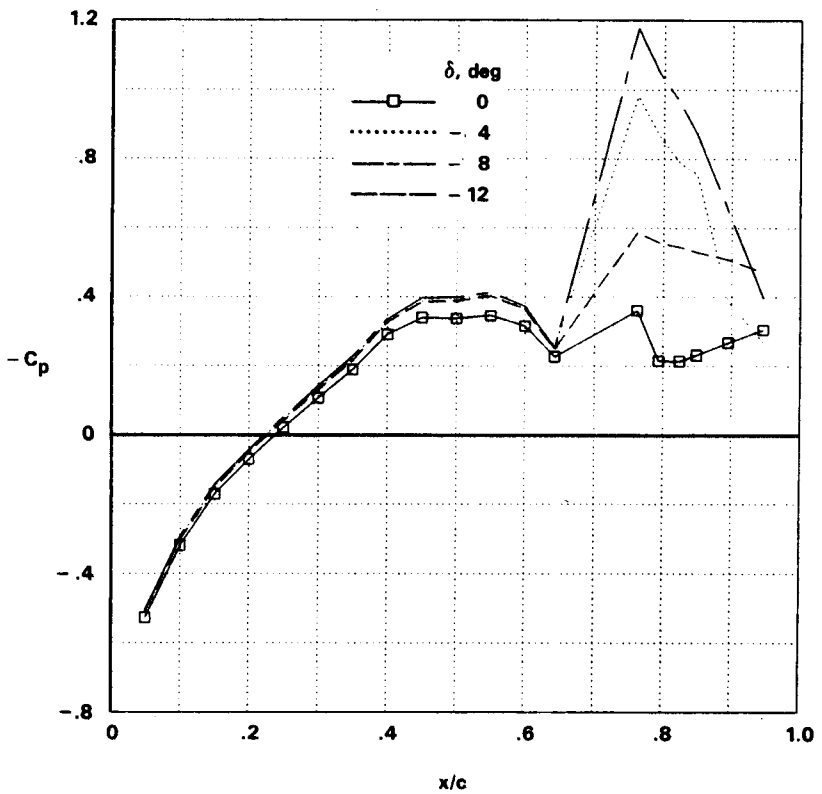

Figure 54.- The effect of flap angle on the lower-surface pressures; M = 0.80, RN = 6.5 million, α = 8°.

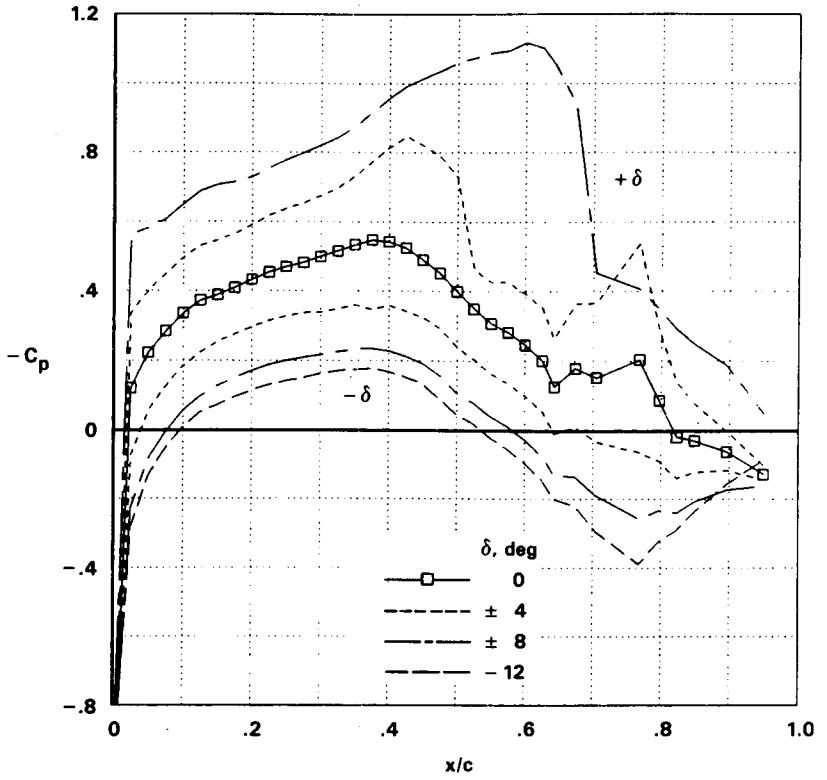

Figure 55.- The effect of flap angle on the upper-surface pressures; M = 0.75, RN = 6.3 million, α = 0.

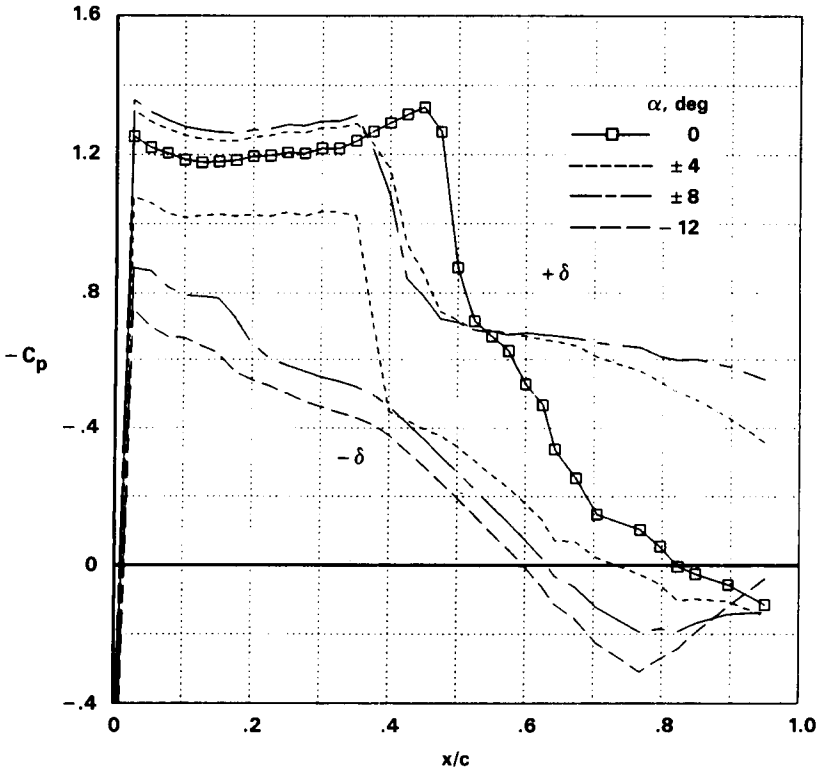

Figure 56.- The effect of flap angle on the upper-surface pressures; M = 0.75, RN = 6.3 million, α = 4°.

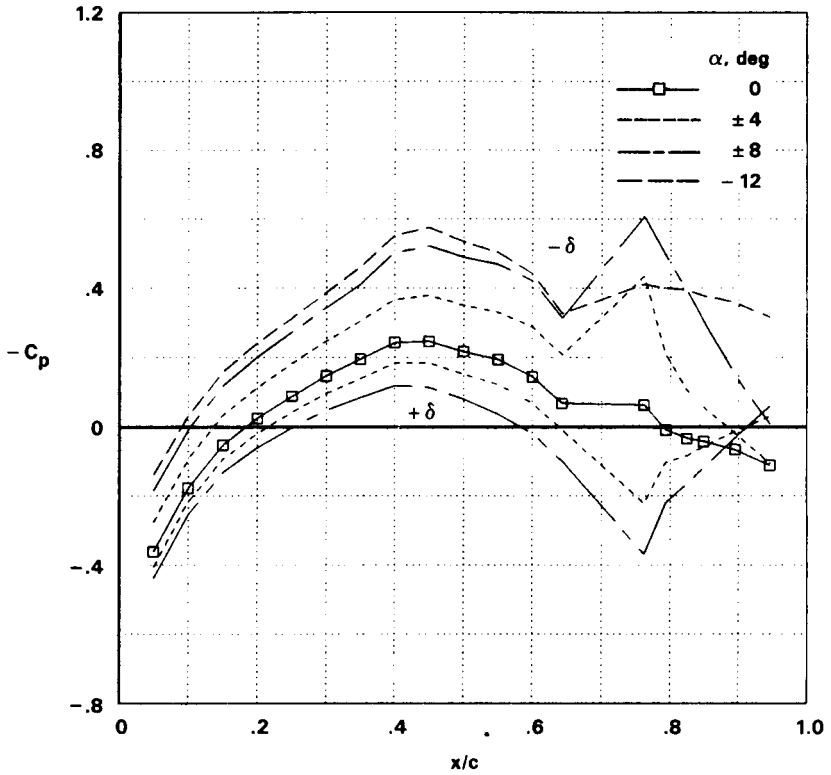

Figure 57.- The effect of flap angle on the lower-surface pressures; M = 0.75, RN = 6.3 million, α = 4°.

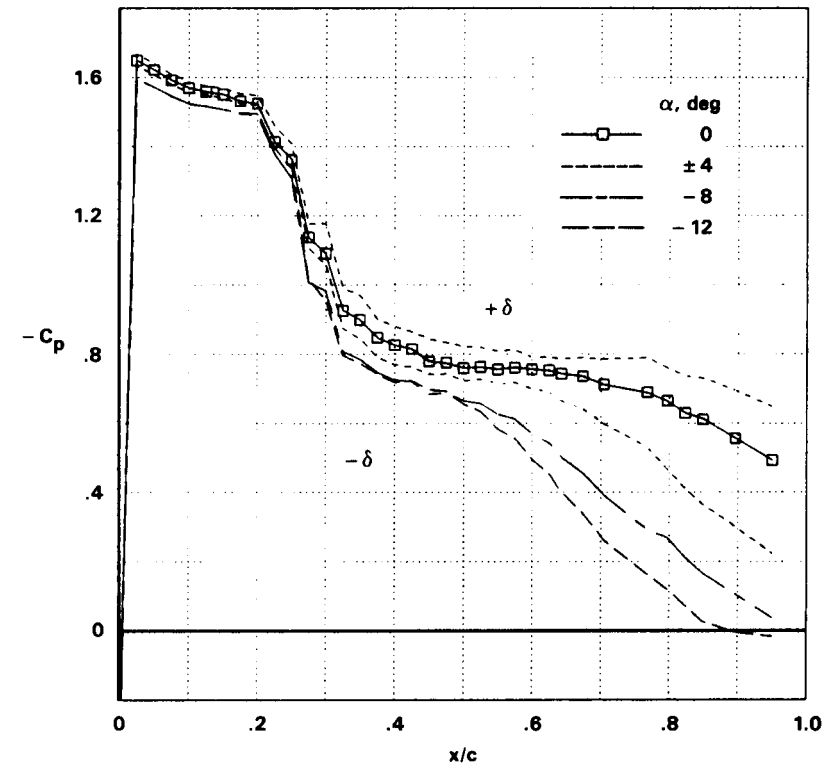

Figure 58.- The effect of flap angle on upper-surface pressure; M = 0.75, RN ≈ 6.3 million, α = 8°.

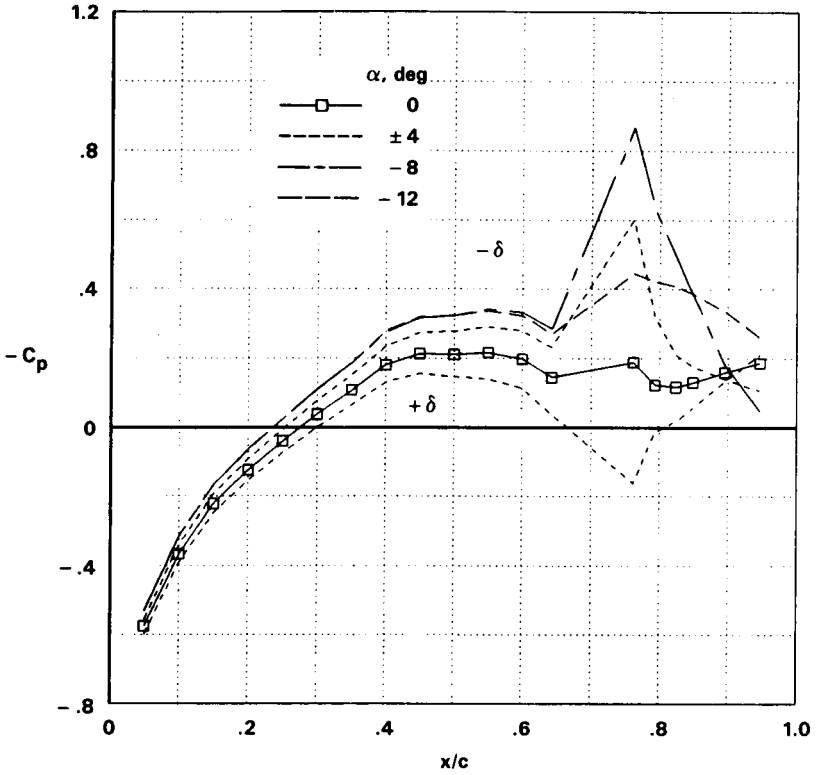

Figure 59.- The effect of flap angle on lower-surface pressures; M = 0.75, RN ≈ 6.3 million, α = 8°.

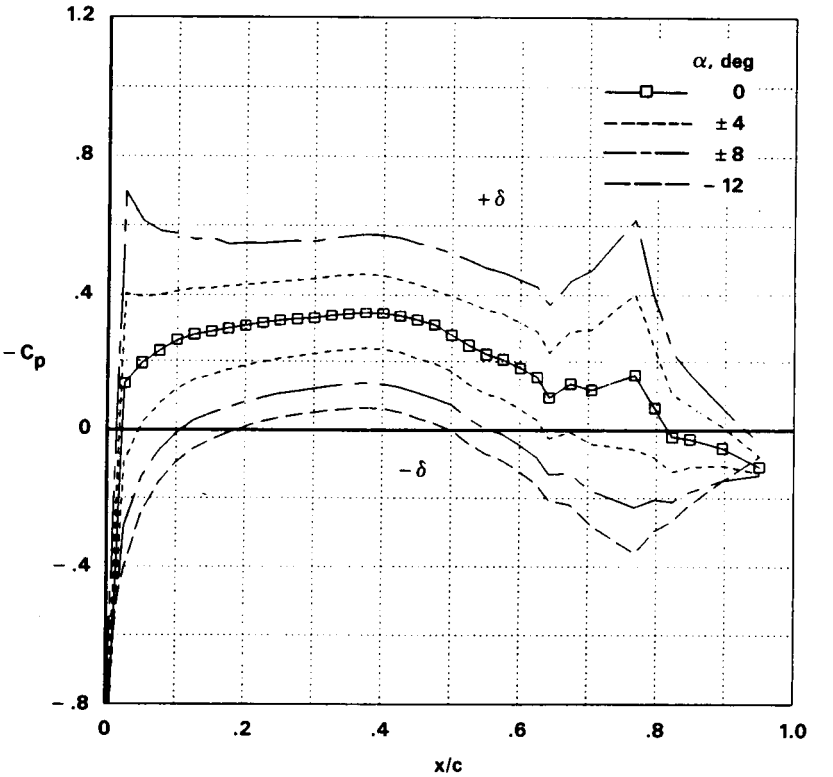

Figure 60.- The effect of flap on upper-surface pressures; M = 0.50, RN ≈ 4.9 million, α = 0.

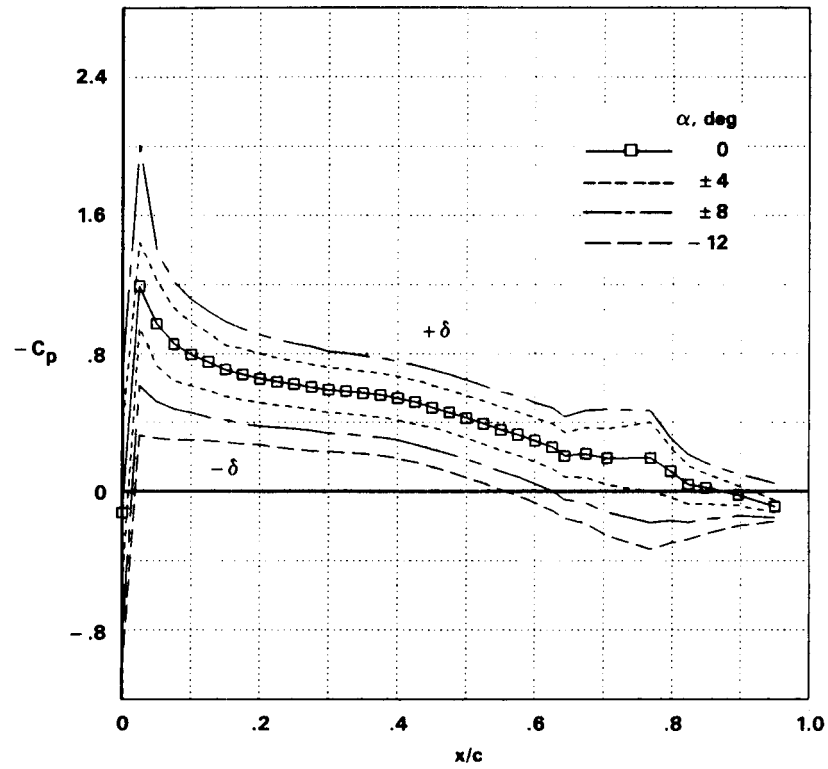

Figure 61.- The effect of flap angle on upper-surface pressures; M = 0.50, RN = 5.0 million, α = 4°.

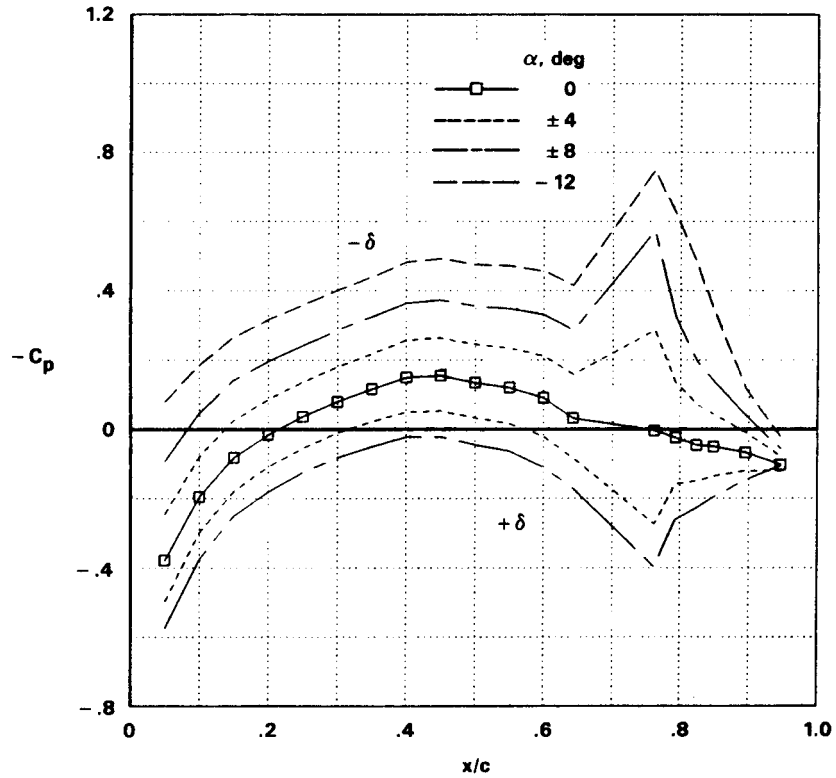

Figure 62.- The effect of flap angle on lower-surface pressures; M = 0.50, RN = 5.0 million, α = 4°.

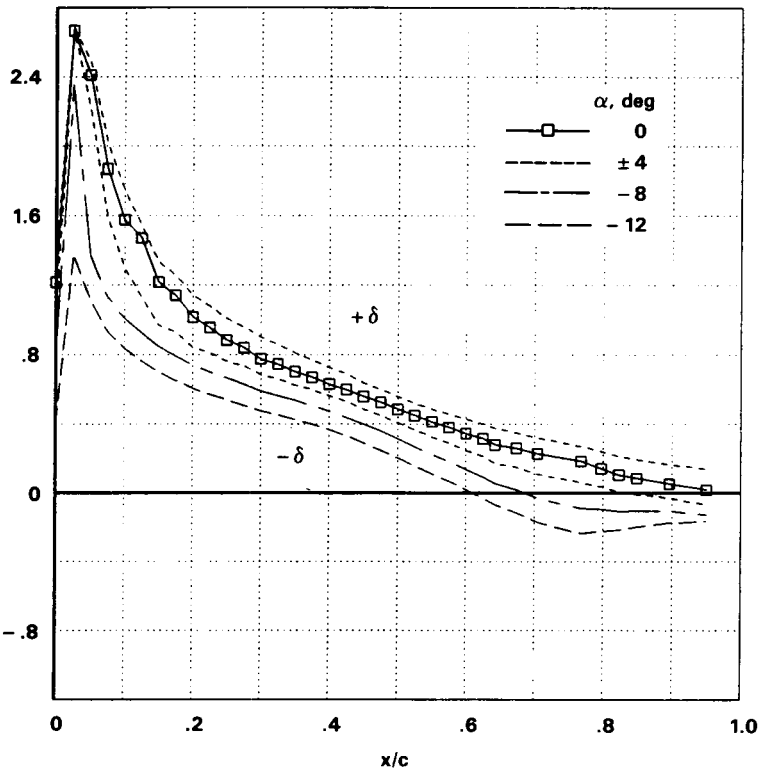

Figure 63.- The effect of flap angle on upper-surface pressures; M = 0.50, RN = 5.0 million, α = 8°.

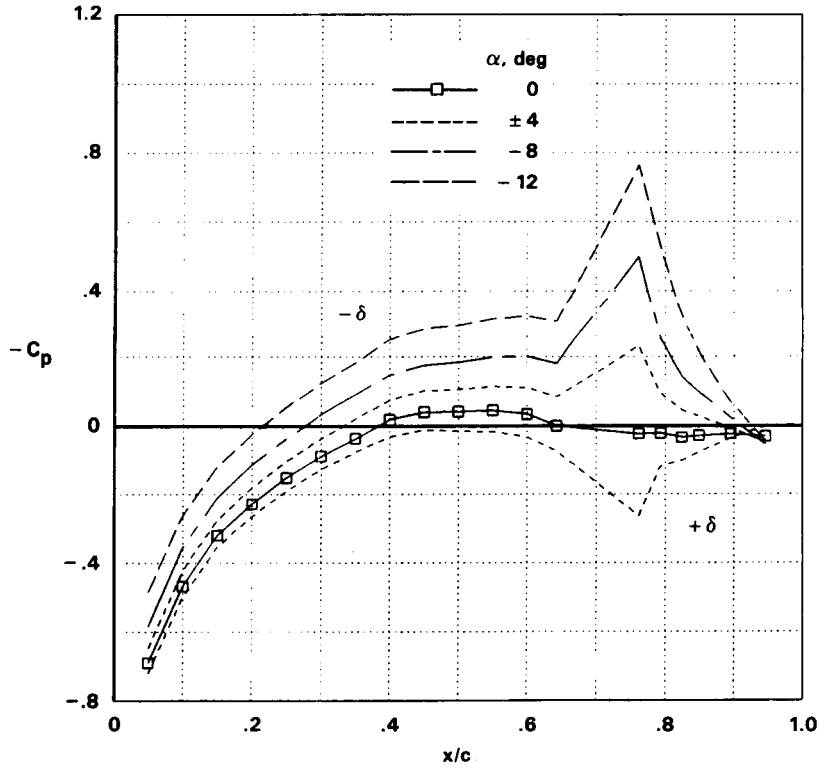

Figure 64.- The effect of flap angle on lower-surface pressures; M = 0.50, RN = 5.0 million, α = 8°.

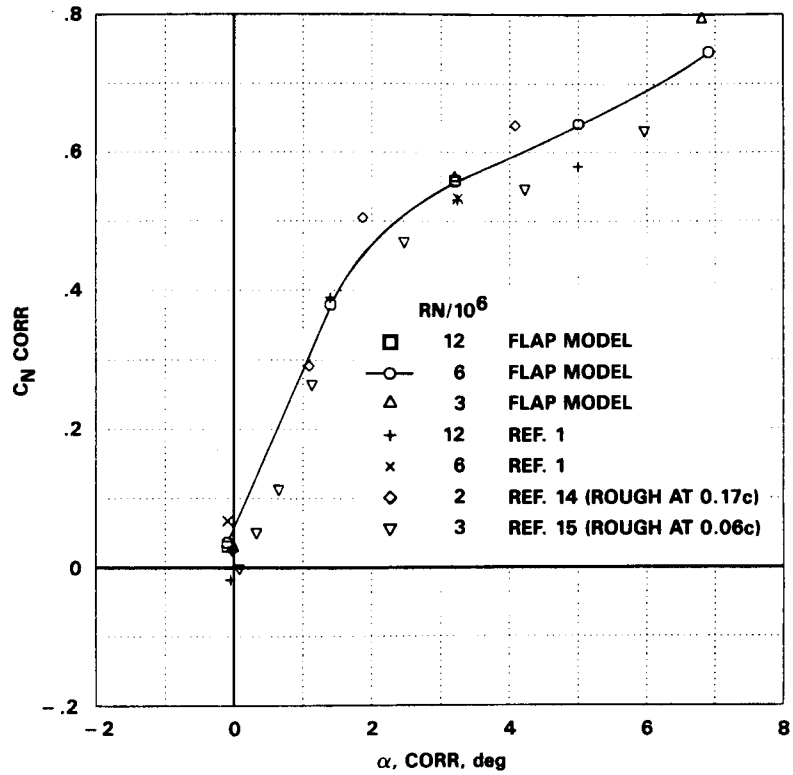

Figure 65.- A comparison of corrected normal-force characteristics with data from unflapped models; M = 0.80, δ = 0.

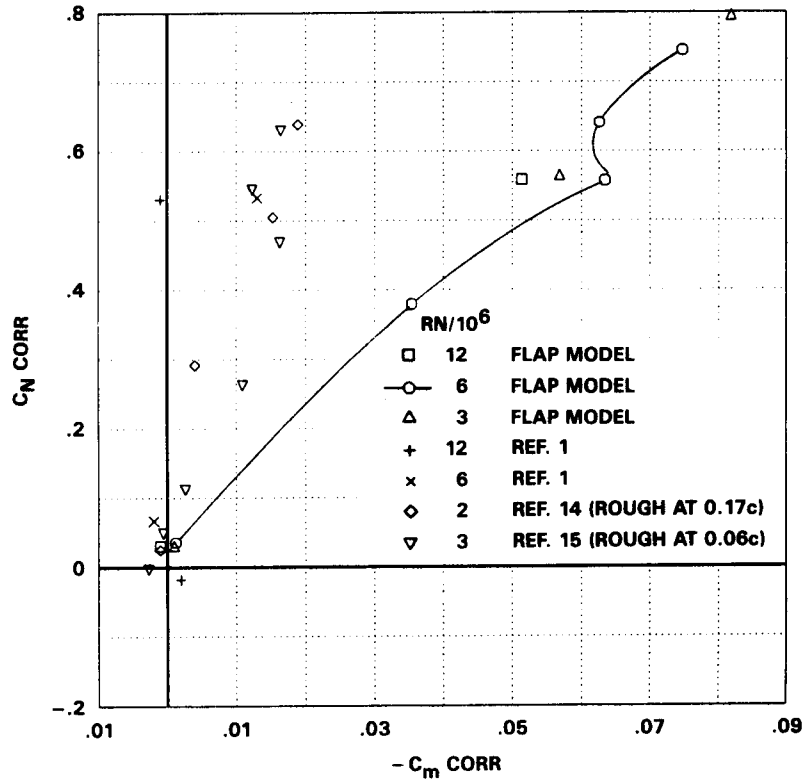

Figure 66.- A comparison of corrected pitching-moment characteristics with data from unflapped models; M = 0.80, δ = 0.

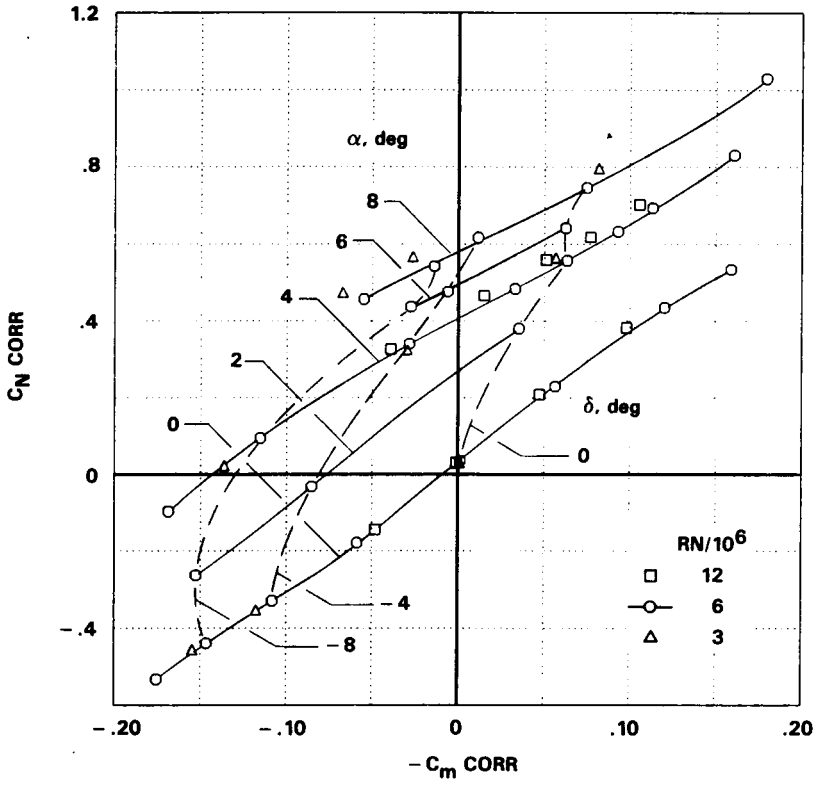

Figure 67.- Pitching-moment characteristics; M = 0.80.

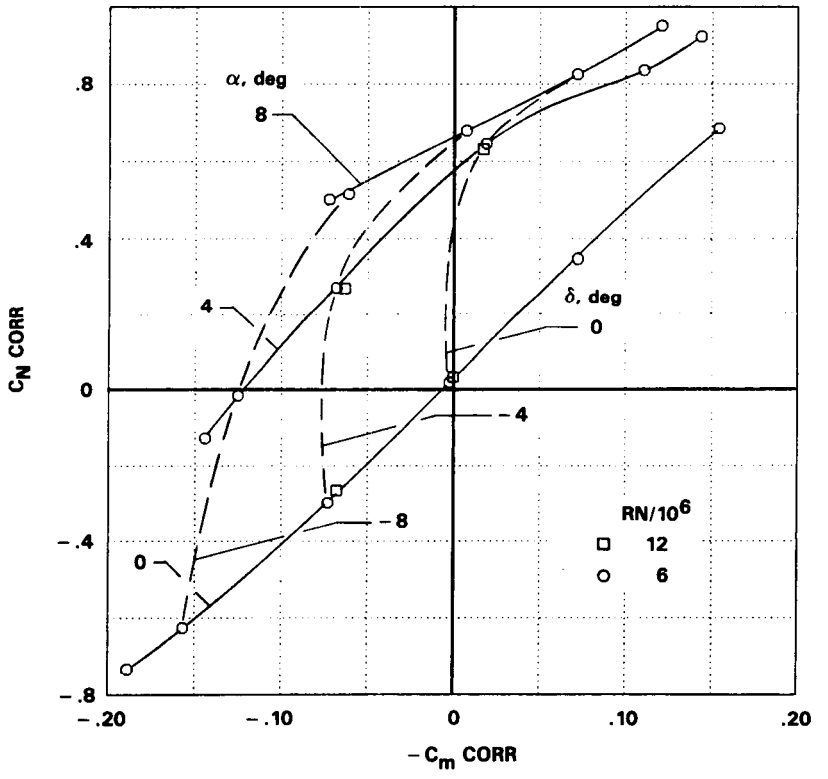

Figure 68.- Pitching-moment characteristics; M = 0.75.

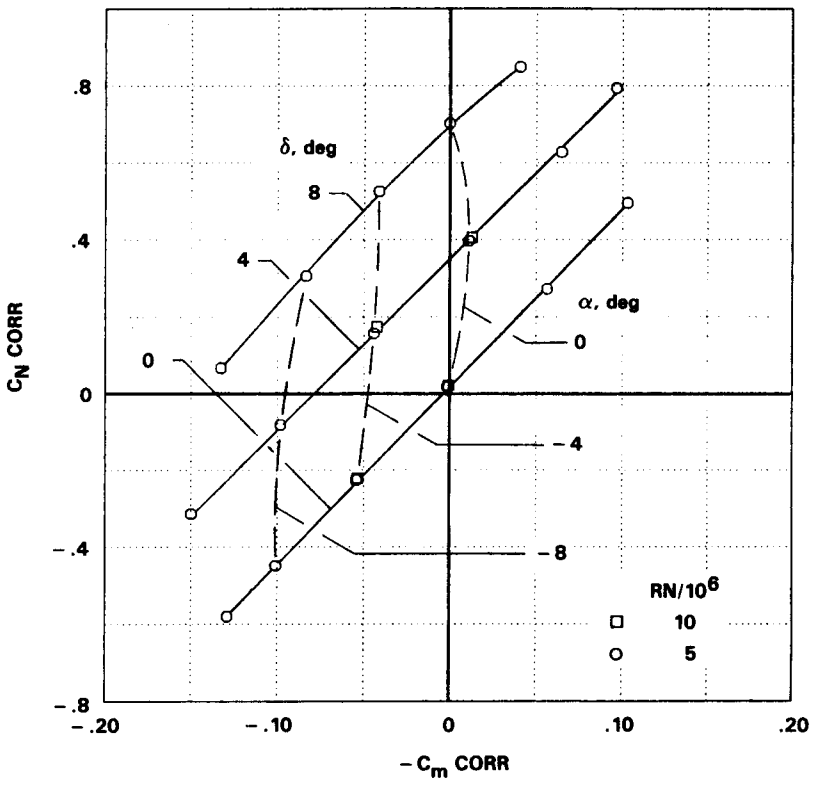

Figure 69.- Pitching-moment characteristics; M = 0.50.

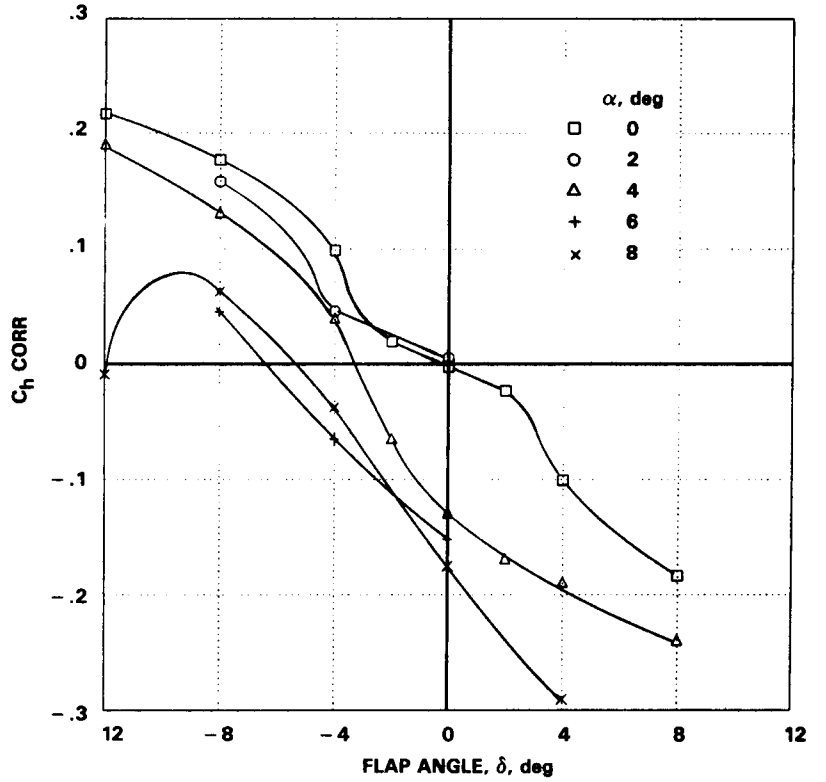

Figure 70.- Hinge-moment characteristics; M = 0.80, RN ≈ 6 million.

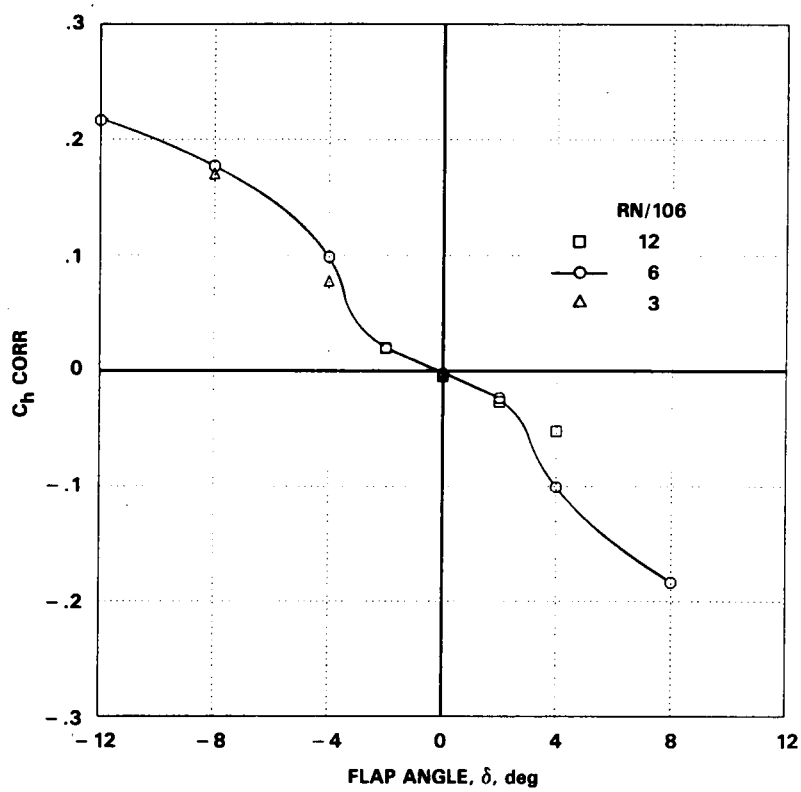

Figure 71.- The effect of Reynolds number on the hinge-moment characteristics; M = 0.80, α = 0.

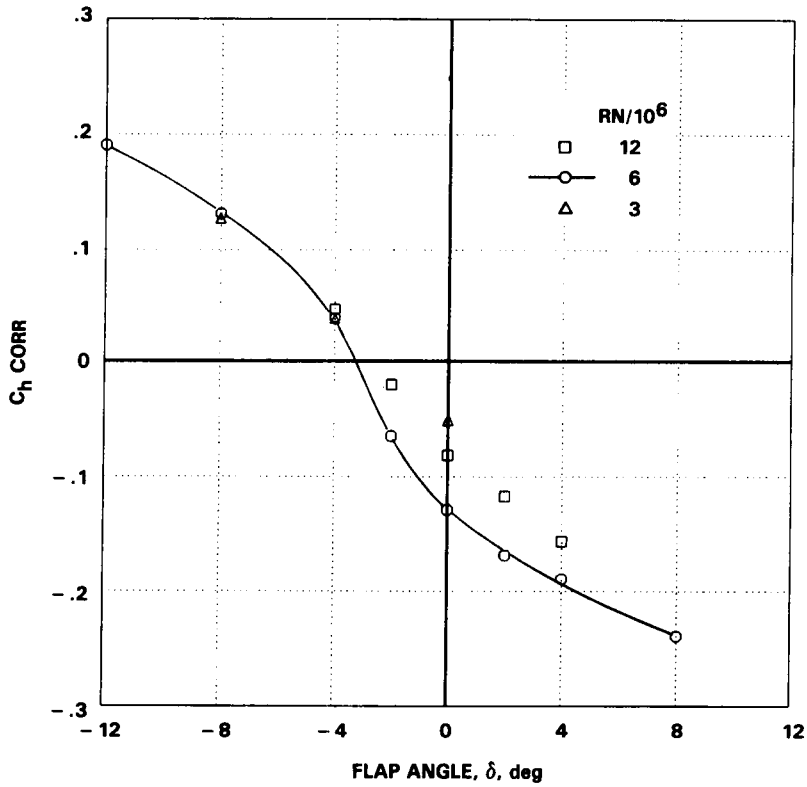

Figure 72.- The effect of Reynolds number on the hinge-moment characteristics; M = 0.80, α = 4°.

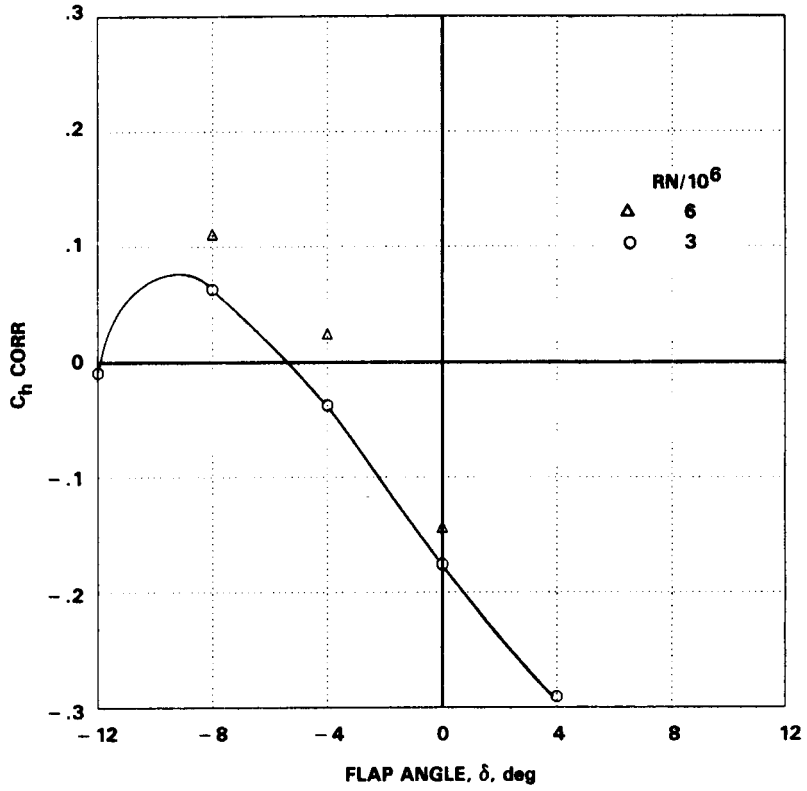

Figure 73.- The effect of Reynolds number on the hinge-moment characteristics; M = 0.80, α = 8°.

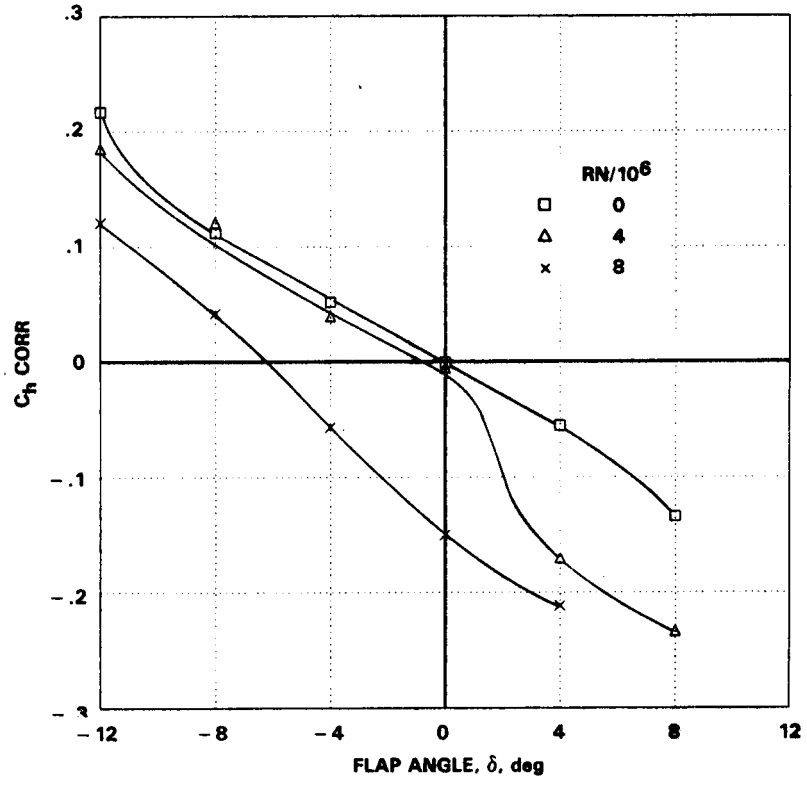

Figure 74.- Hinge-moment characteristics; M = 0.75, RN = 6 million.

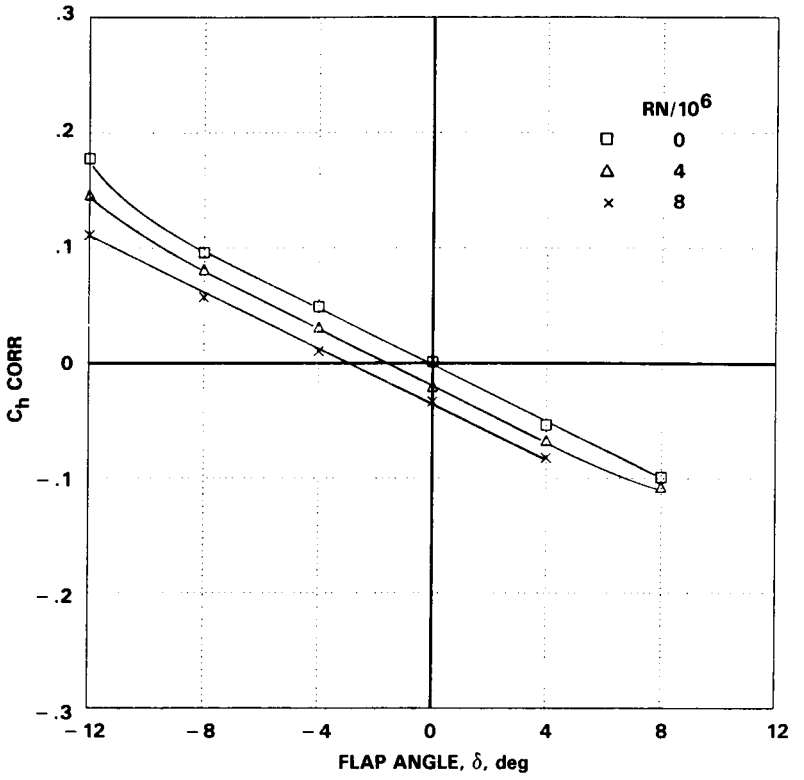

Figure 75.- Hinge-moment characteristics; M = 0.50, RN ≈ 5 million.

1. Report No.	2. Government Accession No.	3. Recipient's Catalog No.
NASA TM-88217		

4. Title and Subtitle	5. Report Date
AN EXPERIMENTAL INVESTIGATION OF THE AERODYNAMICS OF A NACA 64A010 AIRFOIL-FLAP COMBINATION WITH AND WITHOUT FLAP OSCILLATIONS. Part I - Steady-State Characteristics	July 1986
	6. Performing Organization Code

7. Author(s)	8. Performing Organization Report No.
Donald A. Buell and Gerald N. Malcolm	A-86140
	10. Work Unit No.

9. Performing Organization Name and Address	11. Contract or Grant No.
Ames Research Center Moffett Field, CA 94035	
	13. Type of Report and Period Covered
12. Sponsoring Agency Name and Address	Technical Memorandum
National Aeronautics and Space Administration Washington, DC 20546	14. Sponsoring Agency Code 505-31-90

15. Supplementary Notes

Point of Contact: Thomas F. Romer, Ames Research Center, M/S 227-2
Moffett Field, CA 94035 (415) 694-6463 or FTS 464-6463

16. Abstract

A NACA 64A010 airfoil with a sealed-gap 1/4-chord flap was tested between splitter plates in the NASA Ames 11- by 11-Foot Transonic Wind Tunnel at Mach numbers from 0.50 to 0.85, and Reynolds numbers based on chord from 3 to 13 million. Although the main purpose of the test was to obtain unsteady pressure data with the flap oscillating, no unsteady data are presented in this paper. The steady-state data are presented and compared with other test data to provide a basis for evaluating the results.

Pressure data at two span stations are used to deduce early boundary-layer transition at the midspan at higher Mach numbers, angles of attack, and flap angles. The effects of flap angle on pressures, normal force, pitching moment, and hinge moment are also presented in this report. Mach number errors caused by the splitter-plate configuration and the angle of attack are evaluated using pressure measurements near the floor and ceiling of the wind tunnel.

17. Key Words (Suggested by Author(s))	18. Distribution Statement
Airfoil, Control surface, Shock wave, Transonic, Transition	Unlimited Subject Category - 02

19. Security Classif. (of this report)	20. Security Classif. (of this page)	21. No. of Pages	22. Price*
Unclassified	Unclassified	65	A04

*For sale by the National Technical Information Service, Springfield, Virginia 22161